POLITECNICO DI TORINO

Facoltà di Ingegneria
Corso di Dottorato in Fisica

Tesi di Dottorato

Simulation of the propagation of ultrasonic waves for the characterization of complex media

Valentina Agostini

Direttore del corso di dottorato
prof. Mario Rasetti

Tutore: prof. Pier Paolo Delsanto

Quattordicesimo ciclo

Summary

Ultrasonic techniques are one of the most widely used approaches to non-destructive material characterization. In this thesis I have analyzed both linear and non-linear ultrasonic wave propagation in complex materials, i.e. in materials which may present anisotropy, heterogeneities and/or flaws of different kinds (cracks, delaminations,...). The approach to the topic has been numerical throughout my Ph.D. studies.

Computer simulation techniques are continuously expanding their role as basic tools in fields, such as Quantitative Non Destructive Evaluation (QNDE) and Geophysics, in which it is important to gain a good understanding of the propagation mechanisms of waves or pulses in complex media. A method, which has been designed for the above purpose and is particularly efficient, especially in conjunction with parallel processing, is the Local Interaction Simulation Approach (LISA) [1]-[4]. Although it appears formally similar to finite difference methods (FD), LISA is based on a heuristic modeling of local interactions. As spin-offs of LISA, the Sharp Interface Model (SIM) [5] and the Spring Model have overcome [6] the difficulties encountered in treating sharp interfaces or strongly heterogeneous systems by means of the usual FD techniques. The LISA approach has been successfully applied to several linear [7] and non-linear problems [8], showing a good accuracy in reproducing both experimental and theoretical results.

For a quantitative comparison with experimental results it is, however, necessary to properly include in the model the attenuation and dispersion properties of the propagation media. Such effects are seldom negligible in the ultrasonic domain and are required ingredients for the understanding of intriguing effects, such as the hysteretic behavior of rocks and other aggregate systems [9]. Even the prediction of the time-of-flight (TOF's) for a pulse

from a transducer to a receiver may be falsified, when the distortion no longer allows a correct determination of the peak position. Also, in ultrasonic NDE, the knowledge of additional informations, such as the wave-form, the Fourier components, second and higher order TOF's, etc., may be relevant for the inversion.

In the field of material characterization, composite plate-like structures are becoming increasingly important, since they have found basic applications in civil engineering, aerospace, ground transportation, etc. They are often over-designed to compensate for a lack of efficient techniques for testing the initial integrity of the mechanical structures and/or for a reliable monitoring of damage and ageing. Consequently the race for ever improving QNDE techniques (in particular ultrasonic) is still open. Also, considerable attention has been recently devoted to the emerging science of damage assessment, i.e. the combination of ultrasonic excitation with embedded array detection and signature recognition [10].

Established ultrasonic techniques for QNDE take advantage of a wide variety of sources and propagating modes [11]. Surface waves are extremely efficient in probing surfaces and thin plates, since they can propagate a long distance without appreciable attenuation and therefore a large specimen region can be interrogated with a single transducer. In particular, Lamb waves (LW) [12] can explore the entire thickness of a thin plate. The wealth of information provided, however, may be of not trivial interpretation, due to the coexistence of at least two propagation modes [13], in addition to the complexity arising from the heterogeneity and anisotropy of the specimen, its geometry and the presence of defects.

Reliable numerical simulation techniques may be a very valuable tool in this analysis. To this purpose, I investigated the applicability of LISA to the study of the propagation of Lamb Waves in complex structures [14].

In the field of micro-damage diagnostics, nonlinear acoustics has experienced a rapid growth in recent years. In fact, whenever mesoscopic features (i.e. mechanical inhomogeneities, whose characteristic spatial scale is small with respect to the acoustic wavelength, but far exceeds interatomic spacing) are present, acoustic nonlinearity may be up to four orders of magnitude higher than in an unblemished specimen. Correspondingly, nonlinear parameters

are much more sensitive to the properties of micro-inhomogeneities and, in particular, of micro-damage. In fact, nonlinear behavior is observed early on in a degradation process, long before linear parameters start to show damage dependent effects. Any increase in the values of nonlinear parameters is univocally related to an increase in micro-structural features in the material considered.

The interest on the topic initially grew within the field of acoustical geophysics. Multigrained materials such as rocks, sand, soil, concrete, etc., which are collectively called Nonlinear Mesoscopic Elastic (NME) materials, show a rich phenomenology that includes observation from both quasistatic and dynamic experiments. Furthermore a sequence of these experiments performed on numerous materials yields the significant conclusion that damaged atomic elastic materials (such as polycrystalline aggregates with micro-scale damages) behave as NME media. In fact, since they share characteristic properties, they have been conjectured to belong to the same class of NME materials [9]. Therefore they show a far greater non linear elastic response than undamaged ones.

They stand in sharp contrast to materials such as aluminum, diamond and water that have atomic elasticity, which arises from atomic-level forces between atoms and molecules. Materials with atomic elasticity are well described by the classical (Landau) theory of elasticity [15]. However this theory does a poor job when treating the elastic properties of NME materials, which, for low strain levels, are well described by the P-M (Preisach-Mayergoyz) model of non-classical nonlinear elasticity [16].

A very important feature of LISA is the capability of implementing, at a local level, very complex mechanisms, which would be extremely hard to include in a partial differential equation. In fact the method allows full freedom in the choice of the interactions between the nodes, which represent the material cells. It is also possible, by splitting the nodes at the interfaces between different material components, to include at least some of the mesoscopic features and micro-damages discussed before. In fact, all kinds of interactions may be introduced between the subnodes, in which the node has been split, thus simulating perfect or any kind of imperfect contact at the interfaces [6]. Preliminary results, obtained in a collaboration with the

Nonlinear Geophysics Group of the Los Alamos National Laboratory confirm that it is possible to include, in the framework of LISA, classical and nonclassical nonlinear terms, such as those leading to hysteretic or plastic behavior [17].

Text Preview

I begin with a brief introduction of ultrasonic waves, and in particular of their application to Non-Destructive Evaluations of materials in Chapter 1. Chapter 2 describes the LISA simulation method employed to study the wave propagation in solids. Chapter 3 treats the application of the LISA method to the study of Lamb waves in plates. In Chapter 4 the LISA model is modified to be applied to the treatment of NME materials.

Aknowledgements

I wish to thank Dr. P.A. Johnson (Los Alamos National Laboratory, New Mexico, USA), Dr. K.E.Van Den Abeele (Leuven University, Belgium), Prof. R.Guyer (Amherst University, Massachusetts, USA) and Prof. P.P. Delsanto (Politecnico of Torino, Italy) for fruitful discussions. I also wish to thank I. Genesio, D. Olivero and Dr. M. Scalerandi for their day–by-day collaboration.

Special thanks go to my husband, Valentino, and my daughter, Arianna.

Contents

Chapter 1

Ultrasonic wave propagation in solid media

1.1 General background

Ultrasonic wave techniques are increasingly used in areas ranging from nondestructive inspection of materials to noninvasive medical diagnosis. In particular, they are widely used whenever there is the necessity of detecting obstacles in materials that do not transmit light. For example, a low-frequency ultrasonic beam can penetrate many kilometers of the ocean and be reflected back from an obstacle there. This is the principle of sonar[1], which is used to identify submarines, map the ocean bottom, and measure the thickness of ice packs.

Industrially, this same principle is used to detect flaws in solids. When a short pulse of ultrasound is sent into a metal, for example, it is reflected back from any cracks or minute defects such as blowholes. The concept may be extended by the combined use of light and sound in what is called acoustic holography. In this method, an ultrasound beam traveling through water agitates the water's surface. A light beam reflected from this surface is modulated by the pattern of agitation, and the modulated beam can then be used to reconstruct the original sound beam. If the sound beam is first

[1]This technique was developed prior to World War II and inspired early ultrasound investigations.

directed through an object, it is thus possible to reconstruct images of the object's interior.

Fine machine parts, ball bearings, surgical instruments, and many other objects can be cleaned ultrasonically. They are placed in a liquid, e.g., a detergent solution or a solvent, into which ultrasonic waves are introduced. By a phenomenon called cavitation, the vibrations cause large numbers of invisible bubbles to explode with great force on the surfaces of the objects. Film or dirt is thus removed even from normally inaccessible holes, cracks, and corners.

In medicine ultrasonic devices are used to examine internal organs without surgery and are safer to genetic material than x-rays. The waves with which the hard-to-reach body area of interest is irradiated are reflected and refracted; these are recorded by a sonograph for use in diagnosis.

Finally, metals can be welded together by placing their surfaces in contact with each other and irradiating the contact with ultrasound. The molecules are stimulated into rearranged crystalline form, making a permanent bond.

Ultrasonics study the application of the energy of sound waves vibrating at frequencies greater than 20 KHz, i.e., beyond the range of human hearing. The application of sound energy in the audible range is limited almost entirely to communications, since increasing the pressure, or intensity, of sound waves increases loudness and therefore causes discomfort to human beings. Ultrasonic waves, however, being inaudible, have little or no effect on the ear even at high intensities.

1.2 Application to Quantitative NonDestructive Evaluation

NonDestructive Evaluation (NDE) methods evolved from the need to find critical defects in components used in high-risk industries, such as aerospace, railroad and power generation, where failure of a component could have very serious consequences. Nondestructive testing has been practiced for many decades, with initial rapid developments in instrumentation spurred by the

technological advances that occurred during World War II and the subsequent defense effort. During the earlier days, the primary purpose was the detection of defects. As a part of "safe life" design, it was intended that a structure should not develop macroscopic defects during its life, with the detection of such defects being a cause for removal of the component from service. In response to this need, increasingly sophisticated techniques using **ultrasonics**, eddy currents, x-rays, dye penetrants, magnetic particles, and other forms of interrogating energy emerged.

In the early 1970's, two events occurred which caused a major change. The continued improvement of the technology, in particular its ability to detect small flaws, led to the unsatisfactory situation that more and more parts had to be rejected, even though the probability of failure had not changed. However, the discipline of fracture mechanics emerged, which enabled one to predict whether a crack of a given size would fail under a particular load if a material property, fracture toughness, were known. Other laws were developed to predict the rate of growth of cracks under cyclic loading (fatigue). With the advent of these tools, it became possible to accept structures containing defects if the sizes of those defects were known. This formed the basis for new philosophy of "fail safe" or "damage tolerant" design. Components having known defects could continue in service as long as it could be established that those defects would not grow to a critical, failure producing size.

A new challenge was thus presented to the nondestructive testing community. Detection was not enough. One needed to also obtain quantitative information about flaw size to serve as an input to fracture mechanics based predictions of remaining life. These concerns led to the creation of a number of research programs around the world and the emergence of quantitative nondestructive evaluation (QNDE) as a new discipline.

In the ensuing years, many important advances have been made. Quantitative theories have been developed to describe the interaction of the interrogating fields with flaws. Models incorporating the results have been integrated with solid model descriptions of real-part geometries to simulate practical inspections. Related tools allow NDE to be considered during

the design process on an equal footing with other failure-related engineering disciplines. Quantitative descriptions of NDE performance, such as the probability of detection (POD), have become an integral part of statistical risk assessment. Measurement procedures initially developed for metals have been extended to engineered materials, such as **composites**, where anisotropy and inhomogeneity have become important issues. The rapid advances in digitization and computing capabilities have totally changed the faces of many instruments and the type of algorithms that are used in processing the resulting data. High-resolution imaging systems and multiple measurement modalities for characterizing a flaw have emerged. Interest is increasing not only in detecting, characterizing and sizing defects, but in characterizing the materials in which they occur. Goals range from the determination of fundamental microstructural characteristics such as grain size, porosity and texture (preferred grain orientation) to material properties related to such failure mechanisms as fatigue, creep, and fracture toughness–determinations that are sometimes quite challenging to make due to the problem of competing effects.

1.2.1 Ultrasonic techniques

Ultrasonic techniques are one of the most widely used approaches to QNDE material characterization. I resume here some important characteristics of ultrasonic vibrations used in non-destructive testing:

1. they travel long distances in solid materials
2. they travel in well-defined sonic beams
3. their velocity is constant in homogeneous materials
4. vibrational waves are reflected at interfaces where elastic and physical properties change
5. vibrational waves may change their mode of vibration or be subject to **mode conversion** at material interfaces.

The basic task in making mechanical wave measurements is to determine the velocity and attenuation for the particular type of wave under consideration. These measurements may then be related to structural properties of the material. The velocity is primarily a function of the elastic constants and density, while the attenuation is largely determined by dissipative mechanisms peculiar to the type of material, frequency range, grain size, presence of external fields, etc.

Ultrasonic waves are commonly generated by sources made of specially cut crystals of quartz, or ceramics (e.g. barium titanate or lead zirconate). The application of an alternating electrical voltage across the opposite faces of a plate made of such a material produces an alternating expansion and contraction of the plate at the impressed frequency[2]. Ceramic transducers have the advantage of being able to be cast in the form of plates, rings, cylinders, and other special shapes that are convenient for engineering applications. Other ultrasonic transducers are produced in ferromagnetic materials by varying the magnetic-field intensity in the material.

Even though the typical frequency of interest in nondestructive inspection in solid materials ranges from 200 KHz to 20 MHz, there may be special problems requiring an extension of these limits (mechanical wave measurements have been made over a range of frequencies, from less than 1 Hz to approximately 10^{11} Hz). The detail that may be resolved by acoustical waves often depends on the relationship between the wavelength and some relevant structural dimension. For instance, mechanical centimeter and millimeter waves are useful in obtaining information concerning gross structural effects, such as those produced by the grains in a polycrystalline metal or by the dislocations in a single crystal. On the other hand, information concerning effects on an atomic scale requires the use of high-frequency waves.

1.3 Linear elasticity and wave propagation

Any study of the mechanical properties of solids requires at least a nodding acquaintance with basic elastic theory. Therefore in this section I briefly

[2]This phenomenon in crystals, known as piezoelectricity, was first discovered in the 1880s by Paul-Jacques and Pierre Curie.

recall the concepts of stress and strain, and introduce the main vibrational mechanisms observed in solids.

Consider a small volume of a solid body bounded by a surface. In general, two types of mechanical force may act on the body: a) body forces for which the force is proportional to the volume of the body; b) surface forces for which the force is proportional to the area of the surface.

Gravity is an example of the first type of force which involves the force acting on each particle of the body. The stress applied to an elastic body is an example of the second type of force in which the force experienced by the surface particles is transmitted to particles in the interior.

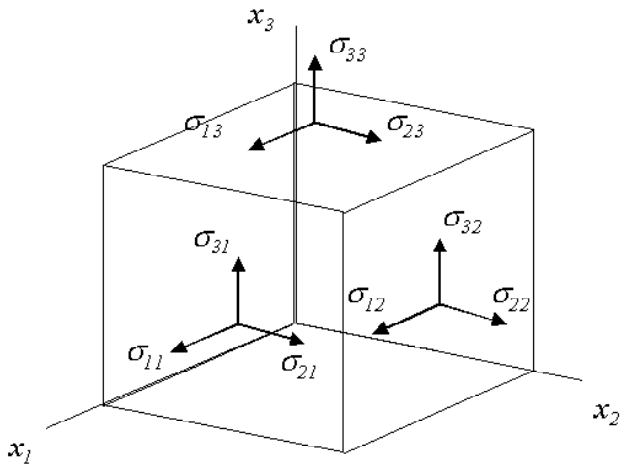

Figure 1.1. The stress components acting on each face of an elementary parallelepiped when a uniform force acts on the body.

Stress may be defined broadly as the force divided by the area on which the force acts. The stress is therefore not only proportional to the direction in which the force acts but also to the orientation of the surface element. Therefore it usual to define a second rank **stress tensor** σ_{ij}, where i and j have the values 1,2,3 (see Fig. 1.1). A double subscript notation is used to identify the components, the first subscript denoting the direction of the stress component and the second subscript denoting the direction of the normal to the plane across which the component acts. It may be shown that the stress tensor is symmetric and therefore there are only six independent

components of stress.

A deformable body is one in which relative motions may occur between its constituent parts giving rise to a change in shape or volume or both. In general, the changes produced by the applied force may be:

1. longitudinal - involving a change in length of the specimen
2. tangential or shear - involving a relative displacement in parallel layers of the materials
3. bulk compressional - involving a change in volume without change of shape.

The deformation is said to be elastic if the body regains its original size and shape after the force are removed. If the applied forces exceed a defined elastic limit, the body will retain a permanent set on removal of the forces. If the forces are large enough, the body may exhibit plastic flow or may fracture.

Let us consider a point P within a solid body whose position coordinates are x_i with respect to a set of Cartesian axes. If P is displaced to a new position $P^{'}$ with coordinates $x_i^{'}$ the displacement vector is defined as

$$u_i = x_i^{'} - x_i.$$

It is usual to introduce also the tensor:

$$\varepsilon_{ik} = \frac{1}{2}\left(\frac{\partial u_i}{\partial x_k} + \frac{\partial u_k}{\partial x_i}\right), \tag{1.1}$$

which is called the **strain tensor**. From eq. 1.1 it follows that ε_{ik} is symmetrical and thus, of the possible nine components of the strain tensor, only six components are independent.

Hook's law may be generalized to state that, for a perfectly elastic body, each component of stress is linearly related to each component of strain. Since there are six independent components of stress and six independent component of strain, for the most anisotropic body with no symmetry relations there will be a set of six equations each with six terms and therefore a

total of 36 coefficients. These equations may be written concisely with the use of tensor notation:

$$\sigma_{ij} = S_{ijkl}\, \varepsilon_{kl},$$

where S_{ijkl} is a fourth rank tensor called the **elastic constant tensor** or **stiffness tensor**. It can be shown that - due to symmetry reasons - the most **anisotropic** crystal system has only 21 independent elastic constants, while, for an **isotropic** material the number of independent elastic constants reduces to 2: they are known as Lamé constants λ and μ [18].

In general, acoustics may be defined as the study of time-varying deformations or vibrations in materials. Within a freely vibrating medium, both inertial and elastic restoring forces act upon each particle of the medium. It is the interplay of these forces that produces oscillatory motions in a manner analogous to the free vibration of a macroscopic system of masses and springs. Thus, the elastic restoring forces in a medium may be described as microscopic "spring" forces.

In solids, the particles can:

1. oscillate along the propagation direction, generating **longitudinal** waves

2. oscillate perpendicularly to the propagation direction, generating **shear** (or transverse) waves.

In addition to waves that travel through the bulk of a material, it is also possible to send waves along the surface of a solid. These are called **Rayleigh** waves and, in this case, the material particles vibrates elliptically. Even more complex vibrations of the particles may be observed for waves guided between two parallel surfaces of a plate. They are known as **Lamb** waves and Chapter 3 will be entirely devoted to them.

Chapter 2

The LISA simulation method

2.1 Introduction

Due to the increasing availability of high performance computer facilities, the range of applicability of simulation techniques is continuously increasing. In fact, from one side, a numerical solution can complement a theoretical analysis, when the problem appears too complex for an analytical solution. On the other side, simulation techniques can often replace experimental measures, being a considerably more economical tool.

There exists a very extensive body of literature [19] on computer simulation techniques, and in particular on Finite Difference (FD) methods [20]. They usually yield very satisfactory solutions, except in the case of heterogeneous materials with a large impedance mismatch at the interfaces between different materials. Furthermore, they are generally restricted to the treatment of perfect contact interfaces.

To overcome these difficulties, a method, which is formally similar to FD techniques has been proposed in recent years by P.P. Delsanto et al. [1, 2, 3, 5]. This method, the Local Interaction Simulation Approach (LISA) aims to a direct introduction of local interactions in the ultrasound propagation mechanism. The Sharp Interface Model (SIM) technique, applied in conjunction with LISA, allows the treatment of any kind of inhomogeneity. By imposing the continuity of displacements and stresses at the interface between different media, the iteration equations can be obtained directly for

any kind of interface. If it is a sharp interface (media with very different properties), the resulting equations are more accurate than the ones obtained with FD techniques, for which a smoothing of the interface is needed.

Furthermore LISA is particularly suitable for the implementation on **parallel computers**. Consequently, by using a proper formalism, an optimal speed-up can be obtained (approximately equal to the number of available processors). The most important property, in view of the applications to material studies, is the reciprocal independence of the processors, which can therefore be putted into a one-to-one correspondence with the cells of the specimen, properly discretized. Such a correspondence is at the basis of the LISA technique. The local interaction between cells can be transferred directly to the processors, bypassing the partial differential equations. Generally, the iteration equations can be obtained, at least in the 1-D case, directly from heuristic considerations. The properties of the cells can be introduced in a completely arbitrary way, being possible to define different parameters for different processors.

Finally, it is worthwhile to mention that, although LISA was originally developed within the field of ultrasonic material characterization, it was also successfully applied to different topics, such as the study of diffusion and growth phenomena in biophysics.

The purpose of this chapter is to describe a **Spring Model** [6], which is a spin-off of LISA, designed to extend the treatment of ultrasonic wave propagation to specimens presenting non-contact or flawed interfaces and, after some additional modifications, to attenuative and non linear hysteretic media. The Spring Model, as the name implies, substitutes the problem of ultrasonic pulse or wave propagation in a medium with the "analog " problem of exciting an equivalent set of "tensorial springs ". The method is stable and convergent as long as the equivalence between the two problems is justified. It is also easily parallelizable and therefore amenable to parallel processing [4].

In the next section the Spring Model is introduced (i.e. the equivalence justified) for the 1-D case. The 1-D case is, of course, very elementary. Nevertheless, it is included because it allows us to define in a very natural way the ingredients (external and internal springs, contact quality factor),

which can later be extended to 2-D in Sec. 2.3. An extension to 3-D is straightforward, but omitted here for brevity.

2.2 The spring model: 1-dimensional case

2.2.1 Propagation along a homogeneous rod

A propagation medium may be considered as one-dimensional if it enjoys transverse symmetry. In this treatment, for simplicity, we start assuming as propagation medium a homogeneous rod of unit cross sectional area and discretize it as a 1-D grid. Each grid-point (or node) represents a tiny segment of rod, which I call a "cell", of length ϵ and mass $m = \rho\ \epsilon$ centered upon the node. Each node acts on its two neighbors $i \pm 1$ with forces $F_i^{\pm}$ given by the elastodynamic equations

$$F_i^{\pm} = \Sigma_i^{\pm} = S\varepsilon_i^{\pm} = S\left(u_{i\pm1} - u_i\right)/\epsilon, \tag{2.1}$$

where $\Sigma_i^{\pm}$ is the stress on each of the two cell interfaces, S represents the material stiffness and $\varepsilon_i^{\pm}$ the deformation and u_i the node displacement from its equilibrium position.

Thus the grid may be replaced by a system of springs with rest lengths ϵ and elastic constants S/ϵ. From the equation of motion

$$m\ \ddot{u}_i = F_i^{+} + F_i^{-} \tag{2.2}$$

for each node i, we easily obtain, by discretizing the time and applying the usual FD formalism [20], the iteration equation

$$u_i^{t+1} = 2u_i^t - u_i^{t-1} + c\Big(u_{i+1}^t + u_{i-1}^t - 2u_i^t\Big), \tag{2.3a}$$

where

$$c = \frac{\tau^2 S}{\rho\epsilon^2} \tag{2.4}$$

is the square of the so called Courant's number and τ is the unit time step. The value of c may be chosen almost at will by varying the ratio τ/ϵ. The

problem of convergence and stability of eq. 2.3a is discussed in ref. [1]. It turns out that the best choice is $c = 1$.

2.2.2 Heterogeneous rod. Perfect contact at junctions

Let us now assume that the rod is no longer homogeneous and that, e.g., an interface located at the node i separates two regions of different physical properties S^-,ρ^- and S^+,ρ^+ at the left and at the right side of the node, respectively. If there is perfect (or rigid) contact between the two regions, we split the node i into two infinitely close subnodes i^+ and i^-, each representing a half cell, of length $\epsilon^-/2$ and $\epsilon^+/2$ and mass $m^- = 1/2\rho^-\epsilon^-$ and $m^+ = 1/2\rho^+\epsilon^+$, respectively. We then assume (see Fig. 2.1) that, besides the "external " forces given by eq. 2.1, two "internal" forces $f_i^{\pm}$ act on the two subnodes in order to keep them together:

$$\ddot{u}^- = \ddot{u}^+ = \ddot{u}^{cm}, \tag{2.5}$$

where the center of mass acceleration $\ddot{u}^{cm}$ is given by

$$\ddot{u}^{cm} = \frac{m^-\ddot{u}^- + m^+\ddot{u}^+}{m^+ + m^-} = \frac{F^+ + F^-}{m^+ + m^-}. \tag{2.6}$$

In eq. 2.5 and following ones I will omit the superscript t and i for brevity. Also I assume, in eq. 2.6, that the internal forces are equal and opposite: $f^+ = -f^-$. From the equations of motion for the two subnodes

$$m^{\pm}\ddot{u}^{\pm} = F^{\pm} + f^{\pm} \tag{2.7}$$

and from eqs. 2.5 and 2.6 it follows

$$f^+ = -f^- = \frac{m^+F^- - m^-F^+}{m^+ + m^-}. \tag{2.8}$$

2.2.3 Imperfect contact

Let us finally assume that the contact between the two regions at the interface may be imperfect. Then we assume that the internal forces are still equal and opposite, but no longer given by eq. 2.8, since the two subnodes may acquire

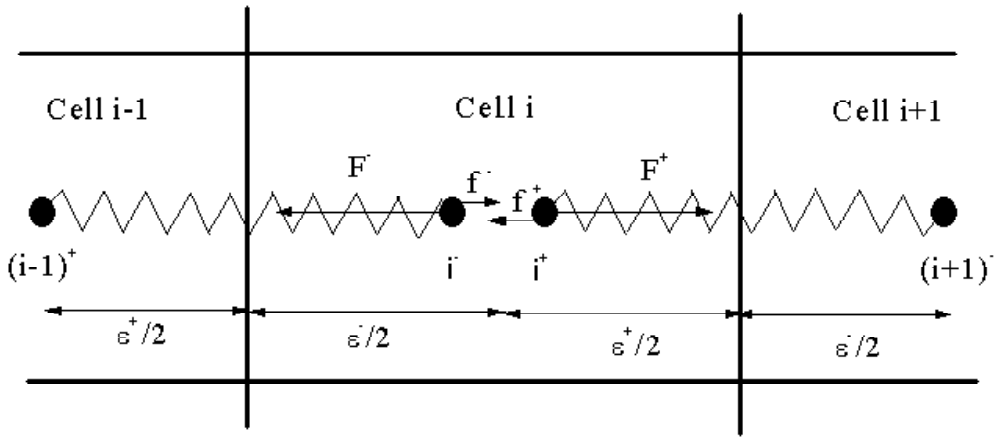

Figure 2.1. Discretization of a rod in a 1-D grid: splitting of the node i into two subnodes $i^+$and $i^-$and representation of the external and internal forces.

some additional degree of freedom. In this case we introduce a parameter Q in the model, to characterize the contact quality at the interface and write the internal forces as

$$f^{\pm} = Q\ f^{\pm}_{pc}, \tag{2.9}$$

where $f^{\pm}_{pc}$ represent the internal forces in the case of perfect contact, as given by the right hand side of eq. 2.8. The contact quality parameter Q may vary from the value $Q = 0$ (delamination or crack) to the perfect contact value $Q = 1$. The bond quality is expected to be connected, although not necessarily in a trivial way, to the contact quality, depending on the physical parameters of the system.

The iteration equations may then be easily obtained:

$$\begin{aligned}\left(u^{\pm}\right)^{t+1} &= -\left(u^{\pm}\right)^{t-1} + 2u^{\pm} + 2c^{\pm}\left(u_{\pm 1} - u^{\pm}\right) \\ &\quad + Qt^{\mp}\left[-c^{\pm}\left(u_{\pm 1} - u^{\pm}\right) + c^{\mp}\left(u_{\mp 1} - u^{\mp}\right)\right], \end{aligned} \tag{2.10}$$

where

$$c^{\pm} = \frac{\tau^2 S^{\pm}}{\left(\epsilon^{\pm}\right)^2 \rho^{\pm}},$$

$$t^{\pm} = \frac{2\rho^{\pm}\epsilon^{\pm}}{\rho^{+}\epsilon^{+} + \rho^{-}\epsilon^{-}}, \tag{2.11}$$

and

$$u_{\pm 1} = u_{i\pm 1}^{\mp}. \tag{2.12}$$

eq.. 2.10 becomes somewhat simplified if, in order to obtain optimal conditions of convergence and stability, ϵ^{+} and ϵ^{-} are chosen to yield $c^{\pm} = 1$. Then we can define the impedance (after and before the interface, respectively) as

$$Z^{\pm} = \sqrt{\rho^{\pm} S^{\pm}} = \frac{1}{\tau}\epsilon^{\pm}\,\rho^{\pm} \tag{2.13}$$

and, as a consequence,

$$t^{\pm} = \frac{2Z^{\pm}}{Z^{+} + Z^{-}} = 1 \pm r, \tag{2.14}$$

where

$$r = \frac{Z^{+} - Z^{-}}{Z^{+} + Z^{-}}. \tag{2.15}$$

eq.. 2.10 then becomes

$$\begin{aligned} u^{t+1} &= -u^{t-1} - 2\ r\ Q\ \delta + (1 + r\ Q)\ u_{+1} + (1 - r\ Q)\ u_{-1}, \\ \delta^{t+1} &= -\delta^{t-1} + 2\ Q\ \delta + (1 - Q)(u_{+1} - u_{-1}), \end{aligned} \tag{2.16}$$

where $u_{\pm}$ are still defined through eq. 2.10 and

$$u = \frac{1}{2}\left(u^{+} + u^{-}\right) \qquad\qquad \delta = \frac{1}{2}\left(u^{+} - u^{-}\right). \tag{2.17}$$

In the perfect contact case ($Q = 1$), $\delta = 0$ and eq. 2.16 becomes

$$u^{t+1} = -u^{t-1} + t^{+}u_{+1} + t^{-}u_{-1}, \tag{2.18}$$

in agreement with Eq.2.3 of ref. [1]. Here t^{+} and t^{-} are the transmission coefficients for the displacement in the forward and backward directions, respectively, and r is the reflection coefficient.

2.2.4 A model for the internal forces

To conclude the Section, it might be useful to attempt a physical interpretation for the internal forces $f^{\pm}$. If we assume that, at the time $t = 0$, $u^+ = u^-$ and $\dot{u}^+ = \dot{u}^-$, from eqs. 2.7, 2.8 and 2.9 it follows that after a time step τ

$$2\delta = \frac{1}{2}\left(\ddot{u}^+ - \ddot{u}^-\right)\tau^2 = \frac{(1-Q)\, f^-\tau^2}{2\ \mu\ Q}, \tag{2.19}$$

where

$$\mu = \frac{m^+ m^-}{m^+ + m^-}. \tag{2.20}$$

We then consider the region (i^-,i^+) as an elastic rod of unit cross section, restlength $\eta \ll \epsilon$ and Young's modulus E. The tiny rod is subject to two concurrent stresses (both in- or outward) f^+ and f^- and to a deformation $2\delta/\eta$. Then

$$E = \frac{|f^+| + |f^-|}{2\ \ |\delta|\,/\eta} = \frac{2\mu Q\eta}{(1-Q)\tau^2}. \tag{2.21}$$

Since μ, η and τ are all infinitesimal of the same order, E has a finite value if $0 < Q < 1$. If $Q \to 1$, $E \to \infty$ and the rod is totally rigid, thus securing a perfect contact at the node i, as expected.

2.3 The spring model: 2-dimensional case

2.3.1 Perfect contact

A propagation medium may be considered as two-dimensional if it enjoys translational symmetry with respect to a given direction (e.g. the z-axis). As an example we consider a material plate of unit thickness and discretize it as a 2-D grid. To consider the most general heterogeneous case, we assume that the physical properties may vary in the lattice from cell to cell, being constant, however, within each cell. Let us assume, for simplicity, that the material has cubic symmetry and call ρ_{ij} the density of a generic cell (i,j),σ_{ij},λ_{ij} and μ_{ij} its elastic constants, corresponding to the cell stiffness components S_{kkkk},S_{kkll},S_{klkl}(k,l = 1,3), respectively.

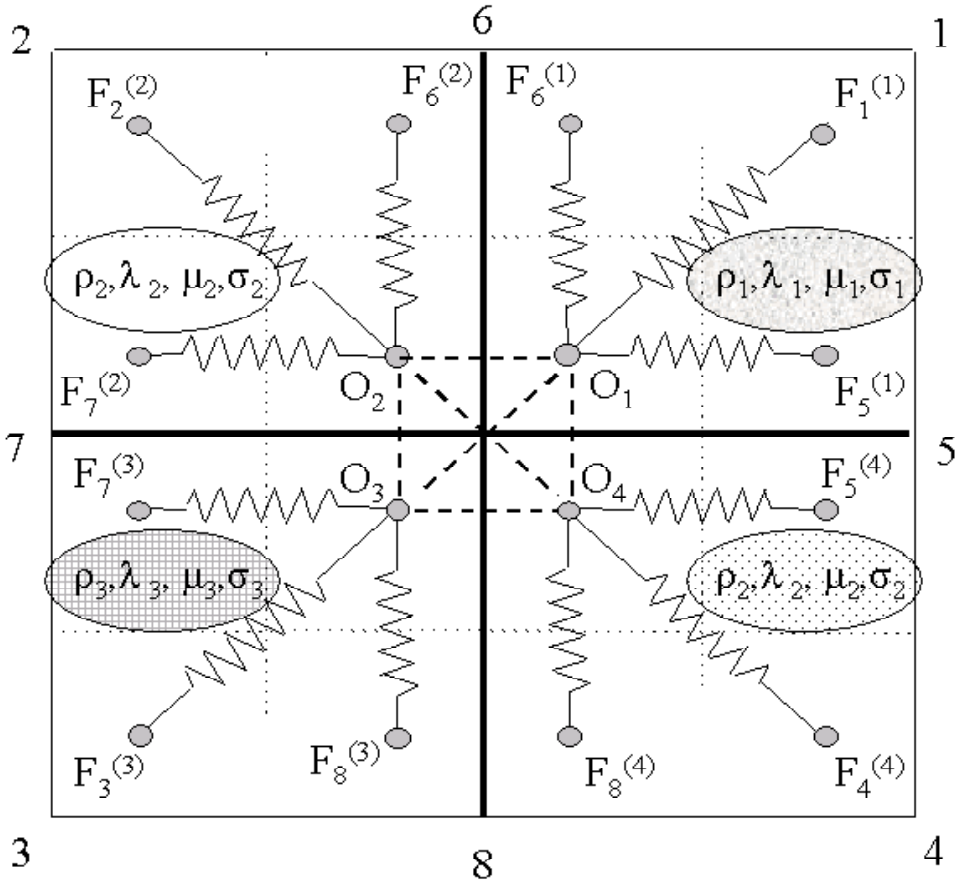

Figure 2.2. Representation of the external and internal forces in 2D.

In order to simulate the propagation, we consider a cross-point $O \equiv (i,j)$ at the intersection between two interfaces separating four different materials, whose physical properties we shall label ρ_k,λ_k,μ_k,σ_k,$k = 1,4$: see Fig. 2.2. Following the treatment of the 1-D case in Section 2.2, we split the cross-point (i,j) into 4 subnodes O_k, each representing a quarter cell in the corresponding quadrant.

For the purpose of simulating the propagation of an ultrasonic wave or pulse, it is possible to prove that the plate is equivalent, in the limit $\epsilon \to 0$, to a system of external and internal springs. The external springs propagate the disturbance of the source pulse throughout the whole grid. Extending to

2-D the procedure developed in Section 2.2 and based on the FD formalism, it is straightforward to obtain an explicit expression for the spring forces $\overline{F}_n^{(k)}$ connecting the subnode O_k to its "nearest neighbor" nodes n

$$\overline{F}_n^{(k)} = M_n^{(k)} \Delta w_n, \tag{2.22}$$

where

$$\begin{aligned} M_n^{(k)} &= \begin{pmatrix} 0 & \psi_k \\ \psi_k & 0 \end{pmatrix} && (n = k = 1,2,3,4) \\ M_n^{(k)} &= \begin{pmatrix} \frac{1}{2}\sigma_k & -\chi_k \\ \chi_k & \frac{1}{2}\mu_k \end{pmatrix} && (n = 5,k = 1,4; n = 7,k = 2,3) \\ M_n^{(k)} &= \begin{pmatrix} \frac{1}{2}\mu_k & \chi_k \\ -\chi_k & \frac{1}{2}\sigma_k \end{pmatrix} && (n = 6,k = 1,2; n = 8,k = 3,4) \end{aligned} \tag{2.23}$$

and

$$\begin{aligned} \Delta w_n &= w_n - w_0, \\ \psi_k &= (-)^{k+1} (\lambda_k + \mu_k)/4, \\ \chi_k &= (-)^{k+1} (\lambda_k - \mu_k)/4. \end{aligned} \tag{2.24}$$

Finally

$$w_n = \begin{pmatrix} u_n \\ v_n \end{pmatrix} \tag{2.25}$$

is the displacement vector of the node n.

If there is perfect contact, the six internal "springs " keep the set of four subnodes rigid, as discussed in the next subsection. Calling $\overline{f}_{kl}$ the internal forces connecting the subnodes O_k and O_l, we assume that

$$\overline{f}_{kl} = -\overline{f}_{lk}.$$

Thus, from the equation of motion applied to the set of the four subnodes, one obtains, after a time discretization (with time unit τ)

$$w_{t+1} = 2w - w_{t-1} + \frac{\tau^2}{\overline{\rho}\ \epsilon^2} \sum_{n,k} M_n^{(k)} \Delta w_n, \tag{2.26}$$

where

$$\overline{\rho} = \frac{1}{4} \sum_{k=1}^{4} \rho_k.$$

In eq. 2.26 I have omitted for brevity the time and/or space subscripts whenever corresponding to the "current " time t or to the node O under consideration. Also note that the masses of the four subcells are $\frac{1}{4}\rho_k\epsilon^2$ ($k =$ 1,4), since they have the same volume $\frac{1}{4}\epsilon^2$. eq. 2.26 is equivalent to eq. 3.18 in ref. [2].

2.3.2 Imperfect contact

In the previous subsection the purpose of splitting the node O into four subnodes was solely due to the need of calculating the spring forces inside a homogeneous region. Thus the forces along the interfaces were split into two separate forces, on either side of the corresponding interface. Following the treatment of the 1-D case in section 2.2, we show notice that such a splitting here has far more outreaching consequences, since it leads to a natural treatment of imperfect contact interfaces.

In order to maintain the set of four subnodes rigid, as required in the previous subsection, it is necessary that the acceleration of each subnode be equal to the acceleration of their center-of-mass

$$\ddot{w}_k = \ddot{w}_{CM} = \frac{1}{\overline{\rho}\ \epsilon^2} \sum_{l=1}^{4} \overline{F}^l \qquad (k = 1,4), \tag{2.27}$$

where $\overline{F}^l$ is the resultant of the three forces $\overline{F}_n^{(l)}$ directly applied to the subnode l: see Fig. 2.2.

Equation 2.27 may be easily satisfied if, by a straightforward generalization of eq. 2.8, the internal forces are chosen to be given by

$$\overline{f}_{kl} = \frac{\rho_k \overline{F}^l - \rho_l \overline{F}^k}{4\overline{\rho}}. \tag{2.28}$$

Then, in analogy with the 1-D case (eq. 2.9), we may extend our model to the treatment of imperfect interfaces by defining a contact quality tensor Q_{kl} for each node O through the relationship

$$\overline{f}_{kl} = Q_{kl}\ \overline{f}_{kl}^{(pc)}, \tag{2.29}$$

where $\overline{f}_{kl}^{(pc)}$ are the internal forces for the perfect contact case, as given by the right-hand side of eq. 2.28. Of course in such a case $Q_{kl} = 1$, for each k and l.

By varying the values of the various components of the contact quality tensor between 0 and 1, one may model a large variety of interface imperfections. Some of them will be considered in the next section. Furthermore, without any increase of computer time, due to the parallel processing of the simulation, the contact quality tensor may vary arbitrarily from node to node and even be different for the x and y components of the internal forces.

2.3.3 The iteration equations

In the case of imperfect contact interfaces the iteration equations must be run independently for all the subnodes, rather than for all the nodes. Their expressions are

$$w_{t+1}^{(k)} = 2w^{(k)} - w_{t-1}^{(k)} + \frac{\tau^2}{\overline{\rho}\ \epsilon^2}\left(\overline{F}^k + \sum_{l\neq k}\overline{f}_{kl}\right) \qquad (k,l = 1,4), \tag{2.30}$$

where the subscript k denotes the subnode being considered. It should be mentioned, for completeness, that in the expression of the forces $\overline{F}_n^{(k)}$ (see eq. 2.22), included in the forces $\overline{F}^k$, and $\overline{f}_{kl}$,Δw_n must be replaced by the difference between the displacement of the subnode of the node n, closest to the subnode k of O, and the displacement of the latter subnode.

Extending the discussion carried on in subsection 2.2.2 to the 2-D case, it is possible to give a more specific physical interpretation to the internal forces. We omit the corresponding discussion for brevity. We limit ourselves to remark here that both the external and internal forces do not represent real springs, in which the force is proportional to the actual distance between

subnodes, but rather "tensorial springs ", in which the x and y components of the force depend on the corresponding components of their distance.

2.4 Parallel processing

The development of high performance computer machines has allowed to overcome the two main limits present in a numerical approach to the solution of many research problems: the huge CPU time request of certain applications and the insufficient memory resources available. This has lead to a great change in the general approach to numerical physics: computer scientists have moved from a research focused on the mere modelization to a thorough design dedicated to specific applications.

When is it possible to solve a physical problem in terms of parallelism? We can think at **parallelism** as being a natural feature of some problems, and one could ask him/herself if every problem present this peculiarity and when it is possible to take advantage of it. A first requirement is to consider physical systems which are reconducible to a multiplicity of elements, which we call "cells". In some cases those systems present themselves as continuous and, as a consequence, the subdivision in cells is merely formal, being an unavoidable tool for the introduction of numerical procedures. In some other cases the systems are intrinsically characterized by a discrete structure and the portioning out in cells will reproduce this structure in a natural way. This is e.g. the case for a consolidated material, i.e. a material constituted of many grains (see Chapter 4): each grain may be put directly in correspondence with a "synthetic" cell.

However the discretization in cells is performed, it will be possible to simulate in parallel the cell evolution only if they present a certain degree of independence among each other. In the case of wave propagation we assume that the disturbance can move, at each time step, from one cell to the neighboring cells only, leaving unchanged all the other ones. In general, we can speak of systems of interacting particles with a short-range potential, where the interaction is intended in a geometrical sense, i.e. the interaction of one particle do not intervene with all the other particles of the systems, but only with the neighboring ones.

The independence may be exploited to introduce parallel processing in the following way: each cell may be put into a one-by-one correspondence with a processor and its evolution calculated by the processor itself simultaneously with all the other ones. The reciprocal interaction among cells is transferred to an interchange of messages among corresponding processors. Since this operation requires additional computer time, the higher is the independence degree among cells the more convenient is the use of parallel computers vs. serial ones.

Although a physical problem may present a certain intrinsic degree of parallelism, one should notice that it may be very important also the parallelism deriving from the modeling or the particular method chosen to solve the problem itself. Two alternative models can lead to completely different degrees of computational complexity, up to the point that it may be impossible to parallelize one of them. An example in this sense may be given considering the use of implicit rather than explicit FD schemes. In an explicit scheme the unknown variable depends on a combination of values of the variable itself, all evaluated at time $(t-1)$, and its calculation may be performed in parallel over all the grid cells. On the other hand, in an implicit scheme, the described dependence also involves quantities that have to be evaluated at time t, which requires to solve a system of linear equations, thus precluding every possible kind of parallelism.

Chapter 3

Linear techniques: Lamb waves

3.1 Introduction

The majority of ultrasonic NDE techniques in use today employ longitudinal or shear waves for flaw detection and thickness measurement in point-scanning applications. In sheet and tube type material, however, a more rapid inspection technique has been developed utilizing guided wave. Among them, Lamb Waves (LW), which propagate between two parallel surfaces of a plate-like object, has long been acknowledged as a very efficient solution for non-destructive testing in large-area, as they are able to travel relatively long distances without appreciable attenuation, allowing the material between transmitter and receiver to be interrogated.

LW testing is generally complicated by the coexistence of at least two modes at any given frequency (see subsection 3.1.2) and by the strongly dispersive nature of these modes at high frequency. Furthermore, a single and pure Lamb mode may generate a variety of other modes either by interacting with a notch, a delamination and/or whenever other kinds of geometrical discontinuities are present in the material (e.g. thickness variations). As a consequence the output signal becomes richer, but often very difficult to interpret and it may be very important to perform a detailed physical analysis of the propagation mechanism. Reliable 3-dimensional simulations of the described phenomena may be a very valuable tool in this analysis.

Due to the fact that in a plate the thickness is much smaller than the other

two dimensions, extensive parallel calculations are needed, in order to ensure a sufficient number of grid points in all the three directions. To this purpose the LISA method (see Chapter 2) has been applied to simulate - given the wave frequency, thickness and physical properties of the plate material - LW propagation in complex structures with defects. In particular, in the various cases presented in this Chapter, I have examined how the "signature" of the defect, i.e. the difference between the reference and the flawed signals, depends on the damage type and location.

One of the highlights of this method is its the capability of directly following the wave as it propagates through the specimen, recording the spatio-temporal evolution everywhere inside (and on the surface) of the material. Therefore, LISA simulations allow to perform "virtual experiments" which permit a valuable insight in the wave propagation mechanisms, as well as the optimization of the interrogation frequency and propagating modes, the source/sensor location, etc.

The present dissertation focuses on LW propagation in composite structural materials, which are becoming increasingly common in aerospace industry, ground transportation, civil engineering, etc. However I exploited also more traditional polycrystalline materials such as Aluminum.

The high degree of anisotropy of certain composite materials may constitute a serious limitation for conventional simulation methods, while LISA has already shown its capability of treating any kind of anisotropy and other complexities of the material [7, 8]. These may give the opportunity for experimental groups to count on numerical low-cost pre-tests.

In particular, within the Brite Euram project DAMASCOS (Damage Assessment in Smart Composite Structures, BE#97-4213), experimental researchers (in particular INSA Laboratories of Lyon, France, and University of Valenciennes, France) supplied the composite material properties [21] that I used as input values for simulations and, as a counterpart, the numerical output was used as a feed-back for optimization procedures such as those mentioned above [22].

In Section 3.2 I present a review of the results obtained applying the LISA method to LW propagation for damage detection in various cases of interest for NDE. In Section 3.2.1 there is a validation of the LISA method comparing

simulations and experimental results in a simple, well defined case study (a composite plate faulted by a passing-by hole). In Section 3.2.2 I analyze LW detection of notches and sub-surface voids. A more realistic damage type is considered in Section 3.2.3: an impact damage induced delamination failure is examined. In conclusion, I introduce in Section 3.2.4 LW propagation in geometrically complex elements, such as, e.g. T- and Y-junctions in stringer structures.

3.1.1 Guided waves

Bulk waves travel in the bulk of the material - hence, away from the boundaries. However often there is interaction with boundaries by way of reflection and refraction, and mode conversion occurs between longitudinal and shear waves. Although bulk and guided waves are fundamentally different, they are actually governed by the same set of partial differential wave equations. Mathematically, the principal difference is that, for bulk waves, there are no boundary conditions that need to be satisfied by the proposed solution. In contrast, the solution to a guided wave problem must satisfy the governing equations as well as some physical boundary conditions.

It is the introduction of boundary conditions that makes the guided wave problem difficult to solve analytically; in many cases, analytical solutions cannot even be found. Another interesting feature of guided wave propagation is that, unlike the finite number of modes (primarily longitudinal and shear) that might be present in a bulk wave problem, there are generally an infinite number of modes associated with a given guided wave problem. That is, a finite body can support an infinite number of different guided wave modes.

Some examples of guided wave problems that have been solved - and whose solution has inherited the name of the investigator - are Rayleigh, Lamb, and Stonley waves [11]. *Rayleigh waves* are free waves on the surface of a semi-infinite solid. Traction forces must vanish on the boundary, and the wave must decay with depth. *Lamb waves* are waves of plane strain that occur in a free plate, and the traction force must vanish on the upper and lower surface of the plate. *Stonely waves* are free waves that occur at

an interface between two media. Continuity of traction and displacement is required at the interface, and a radiation condition must be satisfied.

Among linear ultrasonic techniques, guided waves have become a critically important subject in NDE. In the next section I will introduce in more details Lamb wave propagation characteristics.

3.1.2 Lamb waves

Lamb waves[1] are a type of ultrasonic wave propagation in which the wave is guided between two parallel surfaces of a plate-like object, i.e. an object which has a thickness lesser than a few wavelengths of the incident wave. Particle displacements and stresses in the Lamb waves occur throughout the thickness of the plate. Their propagation properties depend on the density, the elastic properties and geometrical structure of the inspected object and are also influenced by the thickness of the material d and the wave cyclic frequency f. According to their displacement patterns they can be divided into two types, symmetric Sn and anti-symmetric An with respect to the mid-plane of the plate. At low frequency-thickness products fd only two Lamb modes can propagate, the zero-th order A_0 and S_0, which are often referred to as the fundamental flexural and extensional modes, respectively (see Fig. 3.1).

As the fd product increases more modes can be excited and propagate at different velocities. This can be easily understood looking at the dispersion curves shown in Fig. 3.2 for an Aluminum plate (figure reproduced from ref. [23]).

It is interesting to study wave structure variation as one increases the fd product along a particular mode. A symmetric mode cannot be though of as simply an in-plane vibration mode. As one moves along the mode, the ratio of the in-plane to out-of-plane displacement changes. Of particular note are the changes on the outside surface of a structure. Similarly, the antisymmetric modes cannot be thought of as a mode with only out-of-plane displacement values.

[1] Lamb waves were originally studied by H. Lamb in 1917.

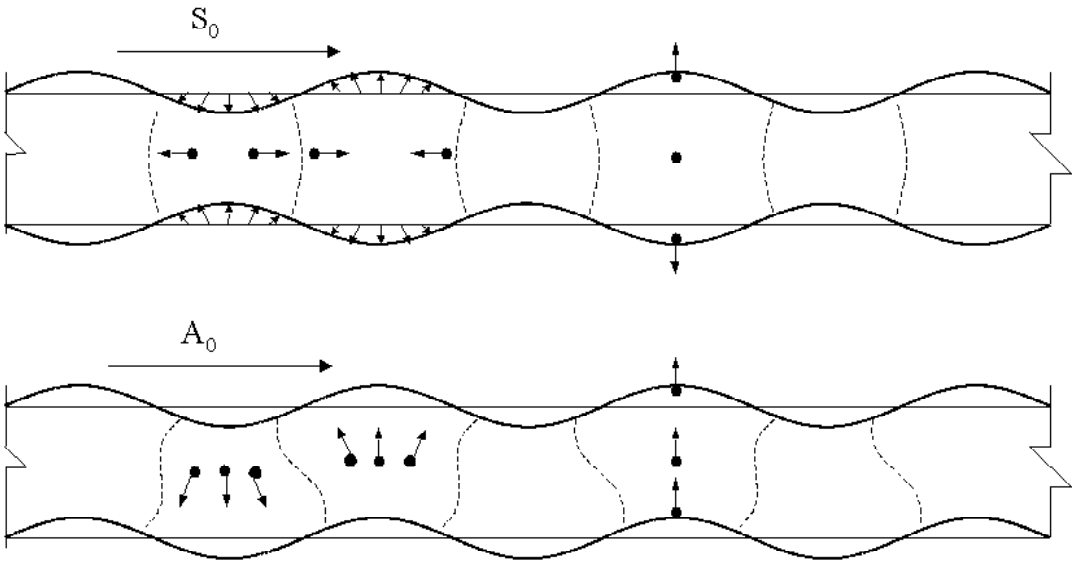

Figure 3.1. Zero-th order symmetric (S_0) and anti-symmetric (A_0) Lamb wave modes

3.2 Lamb wave testing

In this section I demonstrate the applicability of LISA to the study of Lamb wave propagation in complex structures, in particular for the purpose of detection and quantitative evaluation of damages. I analyze several examples of flaws, starting with the simpler case of a passing-by hole, which is considered mostly for the purpose of validating the method (by comparing the results of the simulations with experimental data). In subsection 3.2.2 I consider the more interesting cases of a notch and subsurface flaw; a cone-shaped stack of delaminations is considered in subsec. 3.2.3. Finally, geometrically more complex structures, such as T- and Y- junction stringers are examined in subsec. 3.2.4.

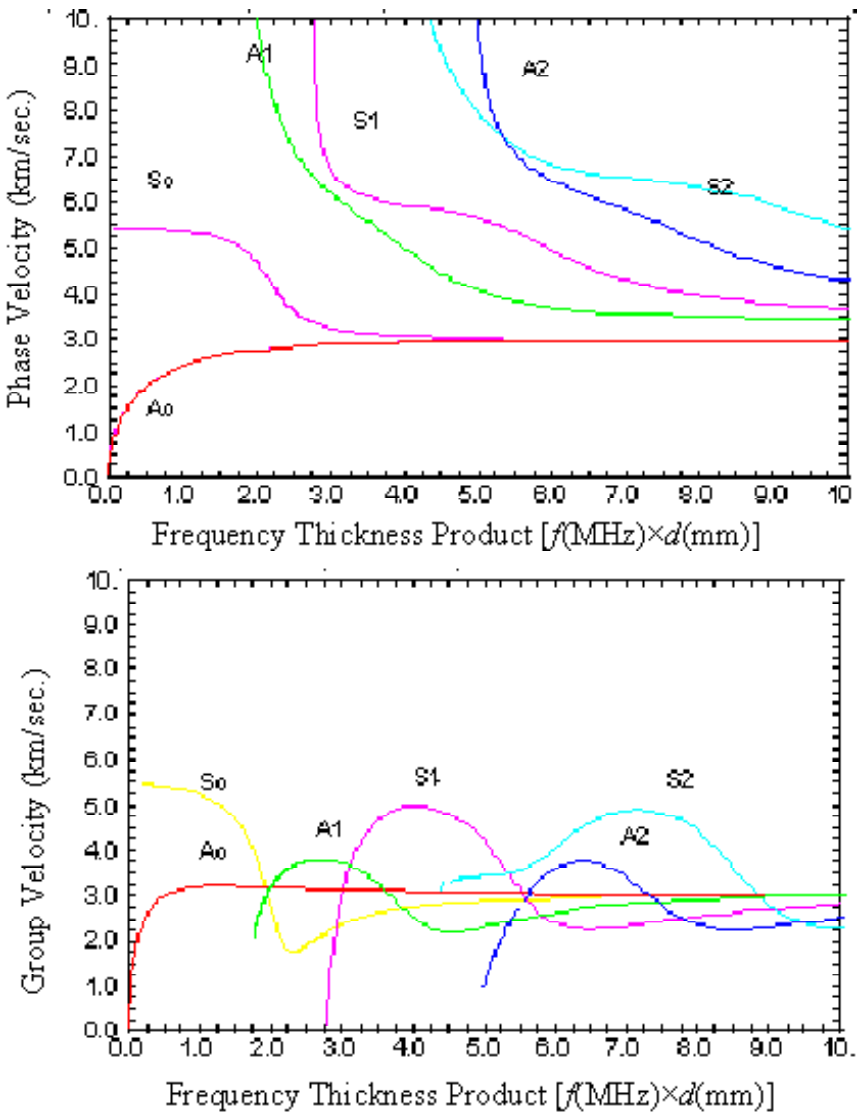

Figure 3.2. Dispersion curves of symmetric and anti-symmetric Lamb Waves in Aluminum.

3.2.1 Damage type: passing-by hole

Let us consider the propagation of LW's through a Glass Fiber Reinforced Plate (GFRP) initially intact and then damaged by a passing-by hole of diameter ranging from 1 to 10 mm. This simple, well defined defect geometry

was chosen in order to validate the simulation method and obtain a quantitative comparison with experimental results in a controlled and reproducible case. It should be noticed that, in spite of its simplicity, this problem requires a 3-dimensional treatment, with a very fine space step ($\ll 3\,\mathrm{mm}$). The ultrasonic source/sensor configuration is schematized in Fig. 3.3.

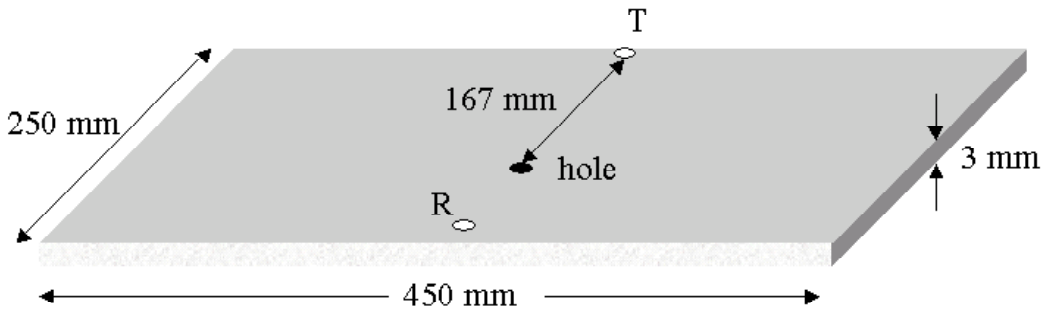

Figure 3.3. Schematic representation of the GFR specimen flawed by a hole. The transmitter T, receiver R and hole location are indicated.

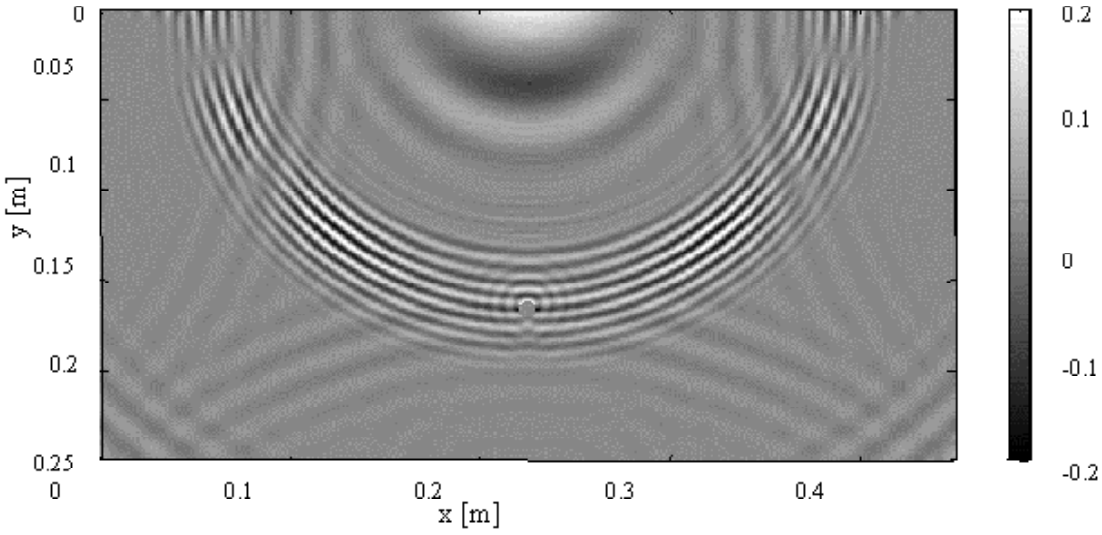

Figure 3.4. Plate flawed by a hole of $\phi = 10$ mm. Map of the out-of-plane component of the displacement at the time $t = 126$ μs.

In order to graphically visualize the wave propagation inside the faulted

material, in Fig. 3.4 we present a snapshot of the LW out-of-plane displacement component in the case of a plate damaged by a 10- mm-hole. In this plot both the S_0 and A_0 modes are visible: the faster S_0 is seen already reflected back from the edge of the plate, while the interference pattern of A_0 with the defect is clearly visible.

A displacement map, such as 3.4, may be quite useful to visualize and understand the propagation mechanisms taking place inside the material, but it is neither sufficient to evaluate the signature of the defect with respect to the reference (unblemished) case, nor to allow a quantitative comparison between numerical and experimental results.

For this reason I present in Fig. 3.5 the S_0 signal collected at the receiver both for the unfaulted plate (upper plot) and for the plate with a 10 mm-hole (lower plot). The latter shows, as expected, a reduced wave amplitude due to partial scattering from the hole. In the plots the continuous line represents the results of our simulations, while the dots refer to experimental data obtained at the INSA Laboratoires (Lyon, France)[21]. We can observe a good quantitative agreement between synthetic and experimental results, although some differences may be noticed at the end of the signals. These are due to the fact that we have not included in our simulations the different transducer damping and material attenuation.

Two major effects originate from the interference of a Lamb wave with a hole: a wave amplitude reduction, due to geometrical dispersion, and a delay in the time signal, due to the fact that the wave travels a longer distance, since it has to circumnavigate the defect.

Both effects can be better appreciated in Fig.s 3.6 and 3.7 (by courtesy of Thomas Monnier), where the S_0 amplitude and time delay are reported as a function of the hole diameter ϕ. The theoretical results (continuous line) agree well with the results of the experiments performed both at INSA (dotted lines) and at the University of Valenciennes, France (dashed-and-dotted lines). It is interesting to note that the S_0 amplitude for $\phi = 1$ mm is slightly higher than when no hole is present ($\phi = 0$ mm). This is due to the fact that we are not considering the whole displacement, but only its out-of-plane component, since that is the quantity measured at the receiver.

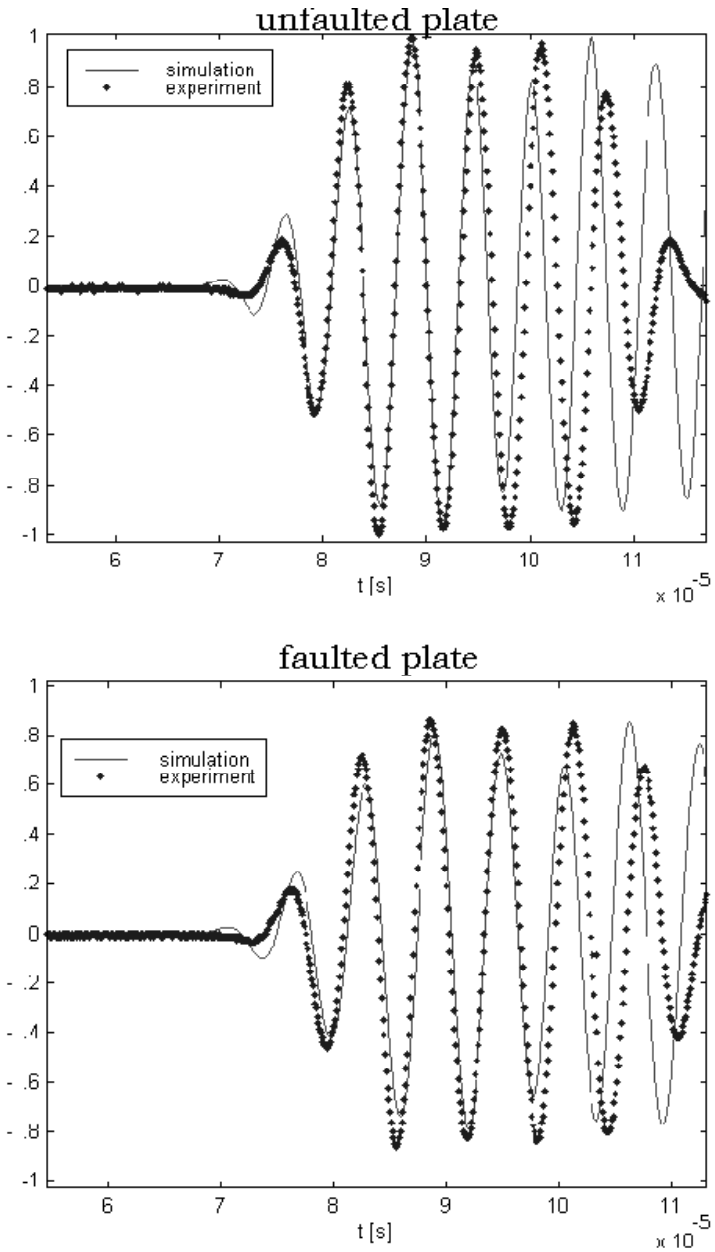

Figure 3.5. Temporal signals at the receiver: comparison between simulations (continuous line) and experimental data (dotted line) for the unfaulted plate (upper plot) and for the plate with the 10 mm-hole (lower plot).

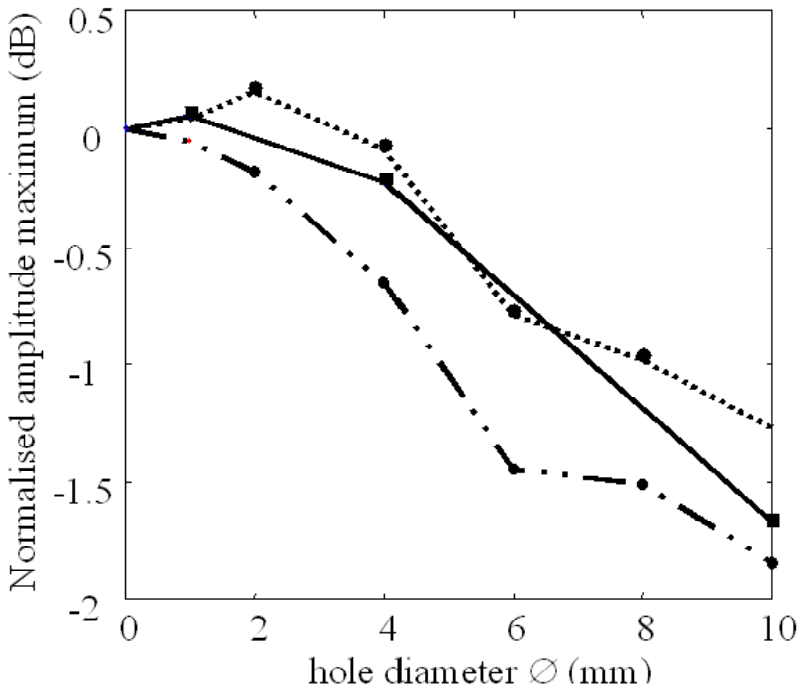

Figure 3.6. S_0 amplitude maximum versus hole diameter in a GFRP. Continuous line: simulation; dotted line: INSA experiment; dashed line: Valenciennes experiments.

3.2.2 Damage type: notch and sub-surface flaw

In this section I analyze the LW's behavior in a plate with a flaw perpendicular to the wave propagation direction. Let us consider an Aluminum thin plate (of thickness d) with a rectangular subsurface defect (void) of length h and width a, located at a depth l from the plate upper surface, as shown in Fig. 3.8. For $l = 0$ we have, as a case limit, a (surface) notch. The reflected and transmitted signals are recorded by two receivers R_1 and R_2 located on the plate surface. They may be used -after a careful analysis of the signature of the defect- for reconstructing the flaw position and shape.

Let us consider the propagation of a zero-th order anti-symmetric Lamb mode A_0 injected from the left side of the specimen containing a surface defect (notch) with $l = 0$,$a = 0.1d$,$h = 0.46d$. In Fig. 3.9 snapshots at four subsequent times of the in-plane (longitudinal) component are shown (note

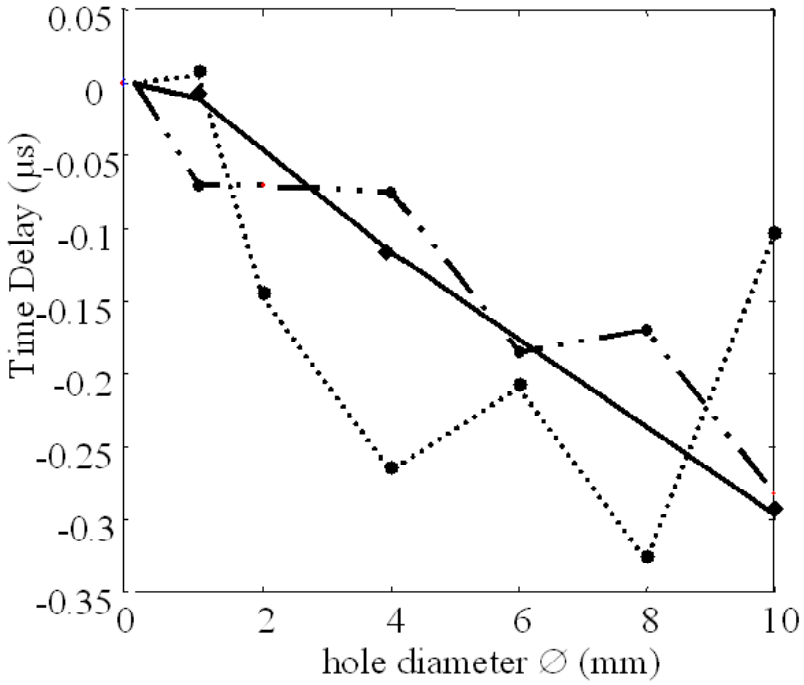

Figure 3.7. S_0 time delay versus hole diameter in a GFRP. Continuous line: simulations; dotted line: INSA experiments; dashed line: Valenciennes experiments.

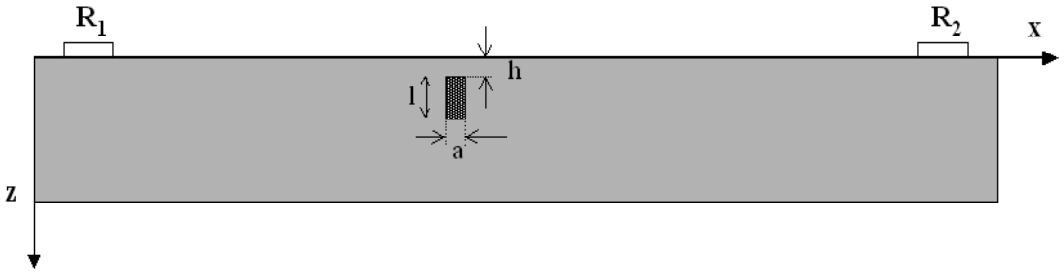

Figure 3.8. Schematic representation of the propagation medium. The darker region represents the defect, R_1 and R_2 represent the two receivers. The emitter is located on the left side of R_1.

the different x-ranges and scales). The uppermost plot displays the pure A_0 mode of the incoming (hanning modulated) wave packet. The second plot

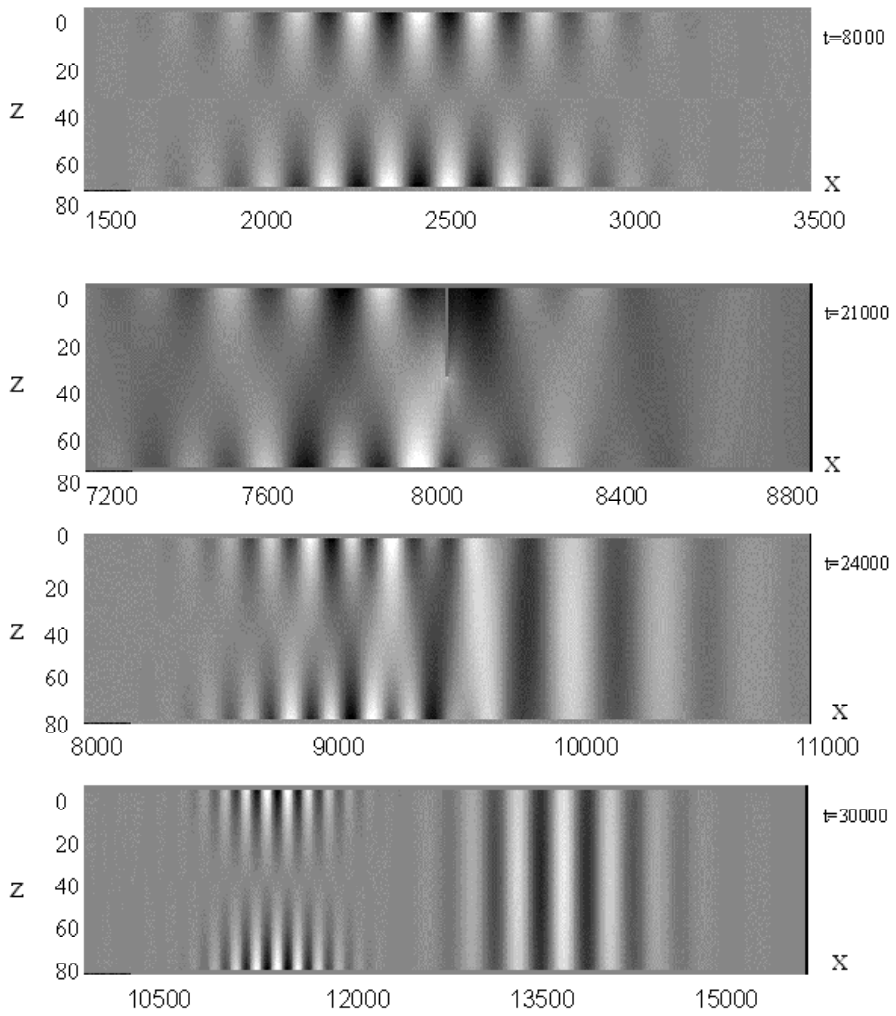

Figure 3.9. Snapshots at various times (in arbitrary units) for a low frequency Lamb mode propagating in an Al plate with a surface notch. Note the different$x$-ranges and scales in the four plots.

shows the scattering effect due to the "breaking" of the wave against the notch. The presence of this discontinuity generates a partial mode conversion from A_0 to S_0. This can be observed in the last two plots, where it is represented the wave transmitted after the notch: in the third one the A_0 and the mode-converted S_0 are still partially overlapping, while in the bottom plot they are well separated. The presence of a mode-converted S_0 mode supplies

additional information, which may be used, as shown later, to predict the defect shape and size. The location of the notch may be easily deduced from the separation (spatial at a given time or temporal at a given location) between A_0 and S_0 (either in the reflected or in the transmitted component) and from the well known phase velocity difference between the two modes.

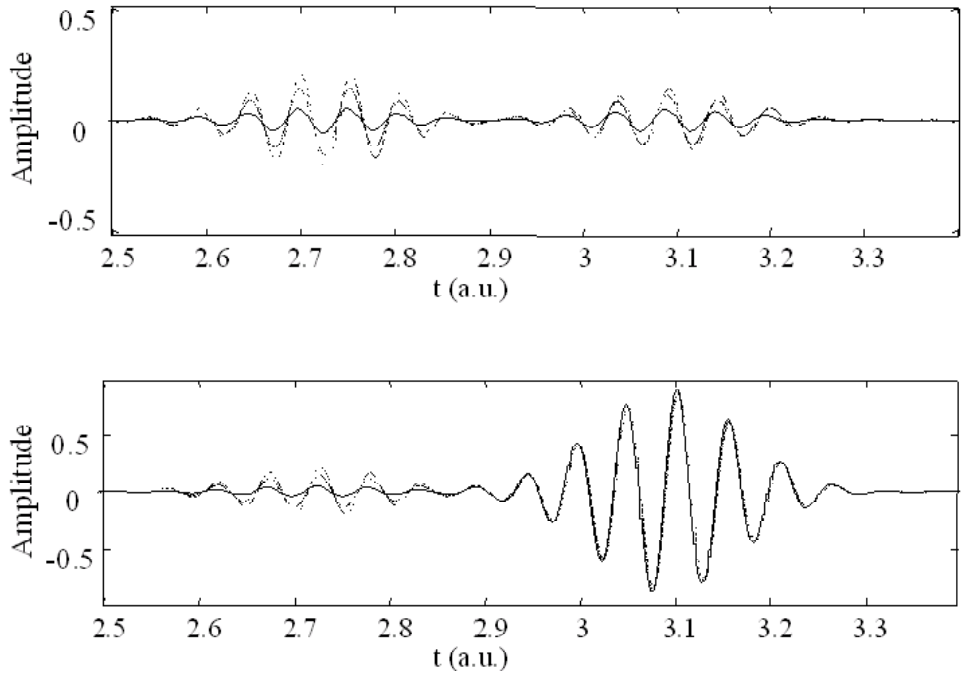

Figure 3.10. Propagation of a LW in an Al plate with a surface defect at different depths: $h = 0.08d$ (solid line), $h = 0.18d$ (dashed line) and $h = 0.23d$ (dots). Longitudinal components of the reflected (upper plot) and transmitted (lower plot) signals.

Again linear plots are needed for quantitative evaluations. In Fig. 3.10 the in-plane (longitudinal) component of the signals received in $R_1$and R_2 (upper and lower plots respectively) are reported vs. time for the case illustrated in Fig. 3.9. The effects of three different depths of the notch are compared. For both the reflected and transmitted pulses we observe first, from the left, the faster mode-converted S_0 pulse and later, trailing behind, the original A_0 pulse. All the pulses, with the notable exception of the transmitted A_0 signal, exhibit a remarkable dependence on h, which can be used

for NDE purposes.

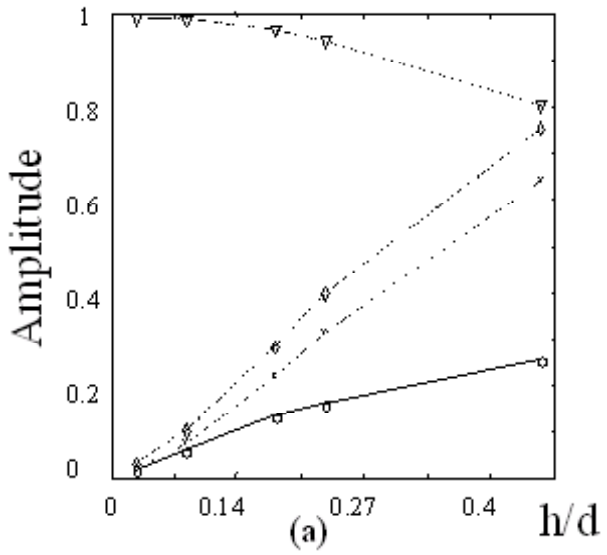

Figure 3.11. Lamb wave amplitudeat a time after the scattering vs. h/d for $l = 0$ (surface flaws). Modes: reflected A_0 (circles), transmitted A_0 (triangles), reflected S_0 (diamonds) and transmitted S_0 (crosses).

In Fig. 3.11 the reflection and transmission coefficients of both the A_0 and S_0 modes are plotted vs. h/d for a surface flaw ($l = 0$). Similar plots for $l \neq 0$ or vs. l/d for a given value of h have also been obtained (omitted for brevity). Measuring the amplitudes of the reflected and/or transmitted Lamb wave modes it is possible, from these plots to deduce h and l and, with a more detailed analysis, to recognize, up to a point, the shape of the defect.

3.2.3 Damage type: delamination

Single delamination

A very common kind of failure in composite plates may be represented as a cone shaped stack of delaminations. I therefore use it to model impact induced damage and proceed to analyze it by means of numerical simulations. In Fig. 3.12 it is shown a sketch of a Carbon Fiber Reinforced Plate (CFRP), which I have studied for this purpose.

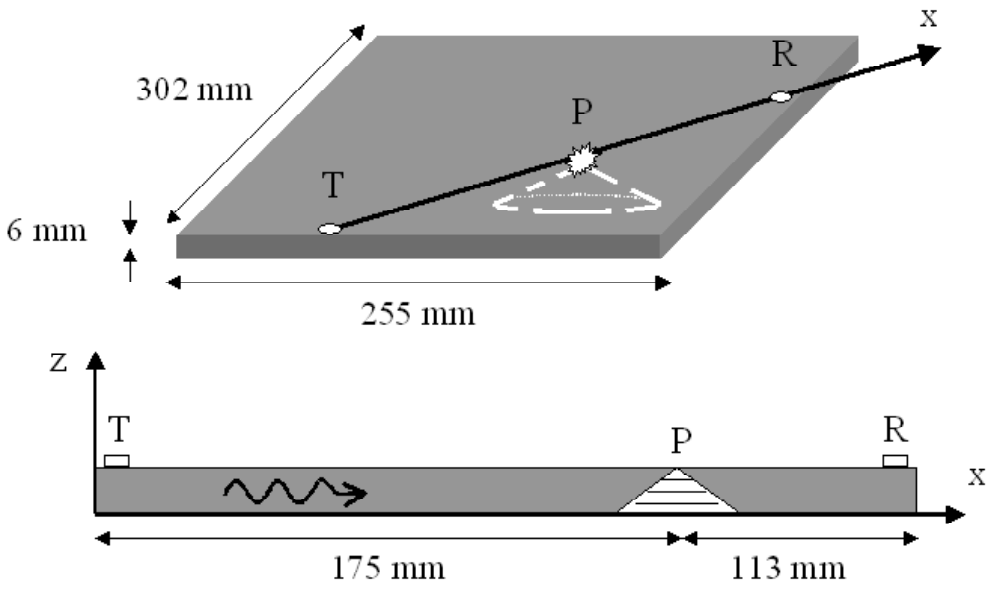

Figure 3.12. Schematisation of the specimen used to study a cone shaped stack of delaminations due to an induced impact (in P). The positions of the transmitter T and of the receiver R are indicated.

In order to prepare the ground for the more complex case under investigation, I consider first a plate flawed by a single delamination. In a virtual experiment we assume to inject from its left edge a hanning-windowed pulse and follow the propagation of the A_0 and S_0 modes thus generated.

In Fig's 3.13 and 3.14 snapshots at two subsequent times are represented of both the in-plane (longitudinal) and out-of-plane (shear) components of the displacement. We recall that in the in-plane u component the S_0 mode is symmetric, while the A_0 mode is asymmetric; the opposite occurs for the out-of-plane v component. In the first two plots of Fig. 3.14 (u component) we notice, proceeding from left to right, first a weak A_0 mode; then, in the delamination region, both the S_0 mode and the mode-converted A_0 (which in the second plot causes the wiggles on top of the smooth and much larger S_0 oscillations), and finally the pure much faster and stronger S_0 mode. Note that in the u component the S_0 mode prevails, while it is almost negligible in the v component. In the third and fourth plots we find first a very strong

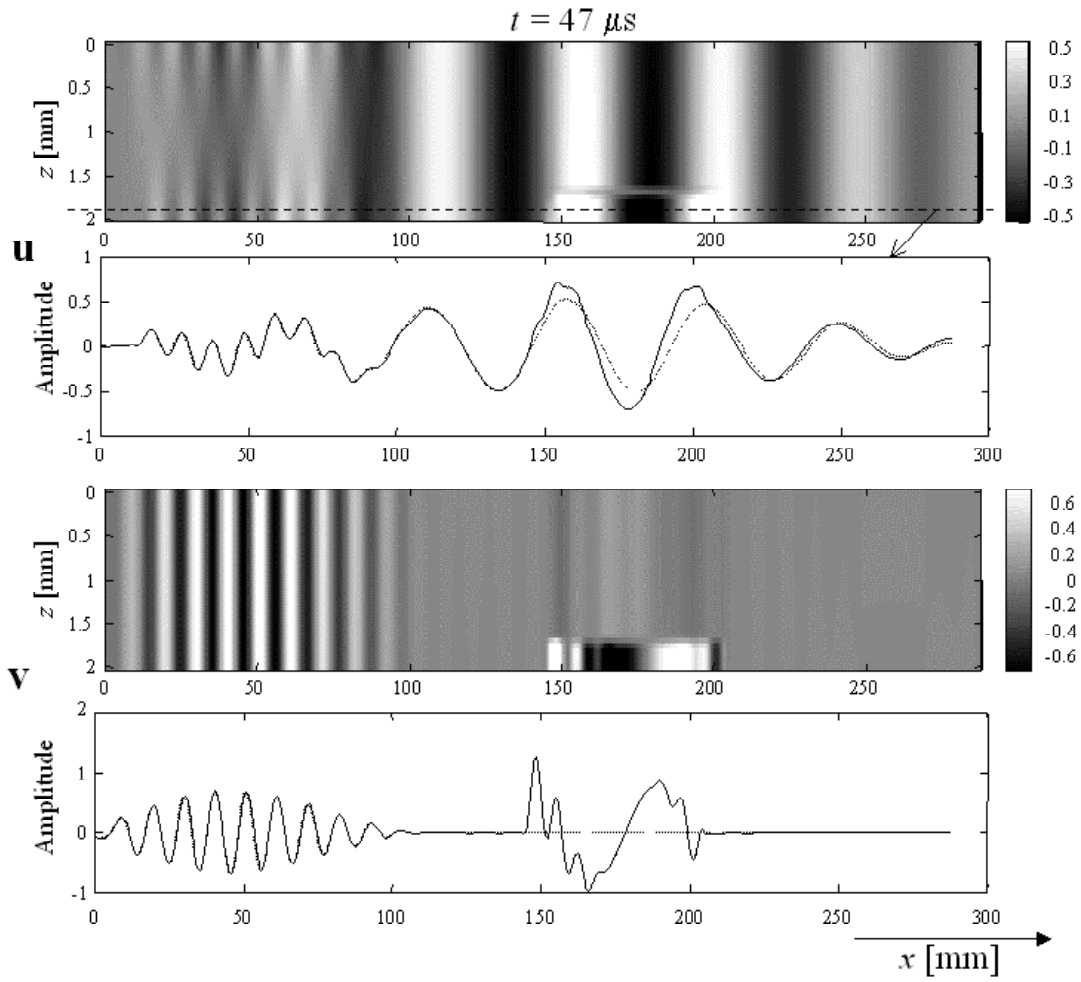

Figure 3.13. Snapshotsof the displacement field at time $t = 47\,\mu$s for a 2-mm-thick CFRP sample flawed by a single delamination of length 6 mm positioned at 0.3 mm from the bottom surface. The first plot represents the in-plane (u) component of the displacement. The second plot shows a section at $z = 1.8$ mm of the upper plot (continuous line) and the respective unflawed case (dotted line). The last two plots represent the out-of plane v component of the displacement.

incoming A_0 mode and then, in the delamination region, a very conspicuous mode-converted A_0 mode (with a different wavelength), which is entirely due to the delamination. In fact it is completely absent in the unblemished plate (dotted line).

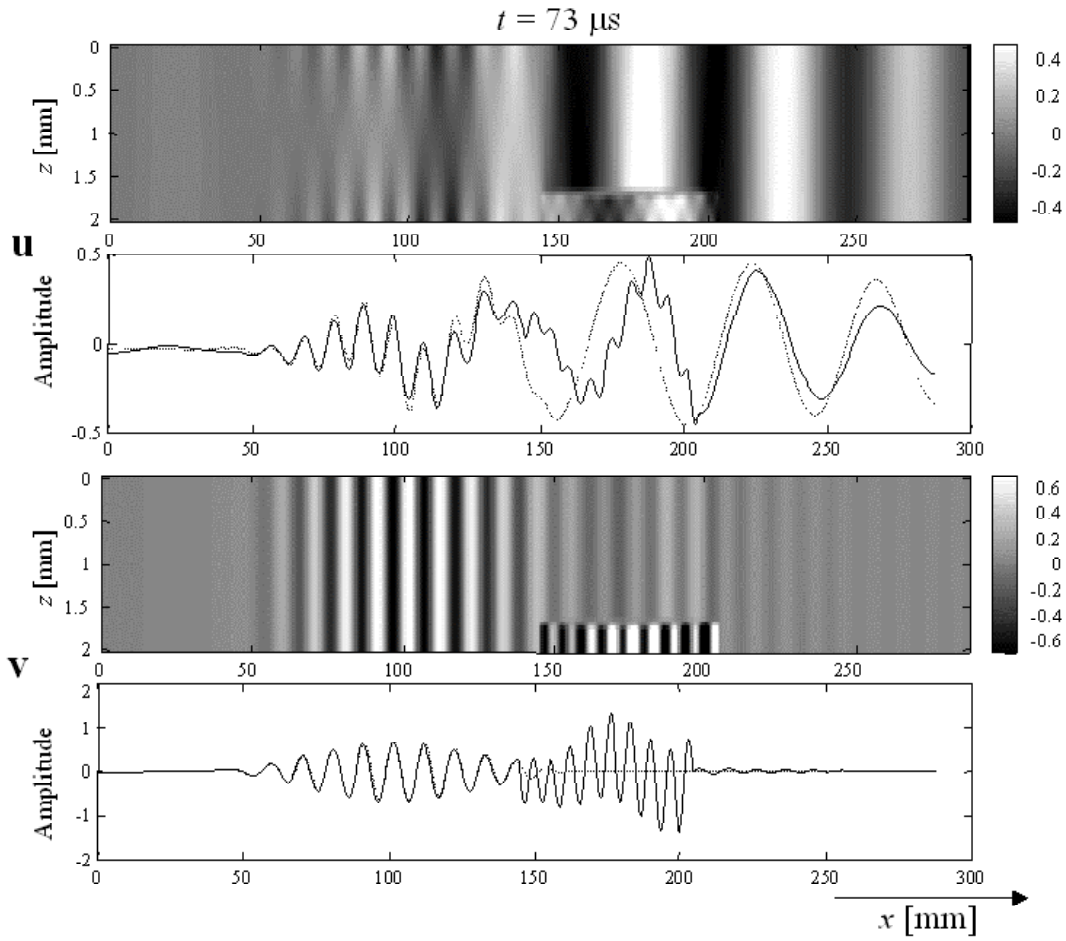

Figure 3.14. Snapshots at time $t = 73$ μs for the same case displayed in Fig. 3.13.

As already mentioned, our simulations technique yields not only the spatial propagation (as shown in Fig.s 3.13 and 3.14), but also the temporal evolution, which is more useful for comparison with experimental data. In Fig. 3.15 we plot the signal, as recorded as a function of time by the receiver, in the case of a 6 mm thick CFRP with a single delamination. Its effect is mostly a time shift (delay) due to the longer path caused by the splitting of the pulse (above and below the delamination) and subsequent recombination.

The dependence on the single delamination position is analyzed in Fig.

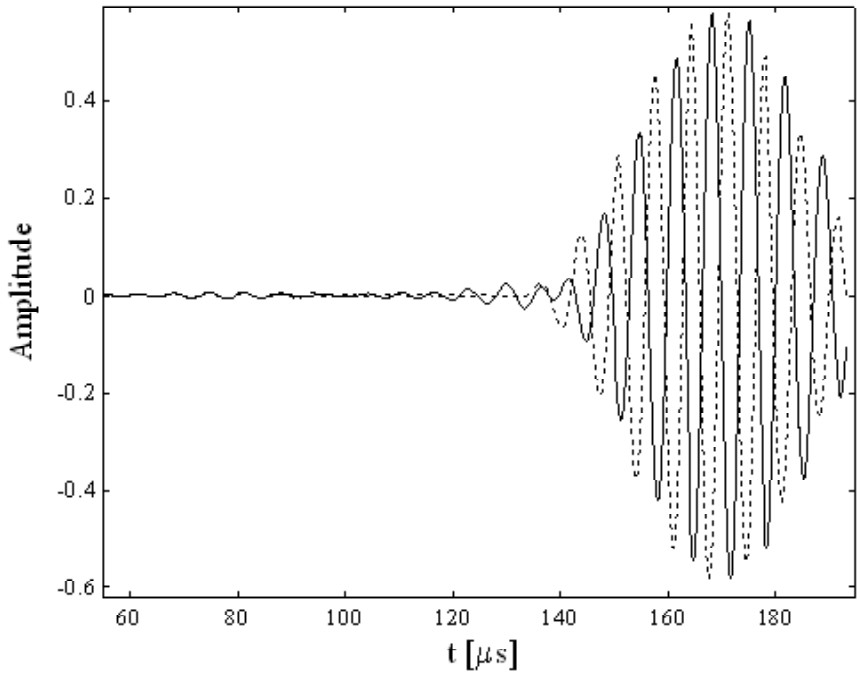

Figure 3.15. Signal collected at the receiver in a 6- mm-thick CFRP with a single delamination positioned at 0.9 mm from the bottom surface (continuous line). The unflawed case is plotted for reference (dotted line).

3.16, which shows both the time delay and difference in peak amplitude (between a flawed and an unblemished plate). Concerning the time shift the effect is larger at mid-plate since, at that location, the pulse is completely broken into two parts and the circumnavigation around the delamination takes the greatest toll. On the contrary, the amplitude difference is larger close to the surface, where the A_0 mode displacement is maximal (thus leading to a greater discontinuity), while it vanishes at mid-plate.

Cone-shaped stack of delaminations due to impact damage

Finally the effect of a cone-shaped stack of delaminations is illustrated in Fig.s 3.17 and 3.18. Fig. 3.17 displays both the u and v components of the displacement in a similar fashion to Fig.s 3.13 and 3.14. The effects of the

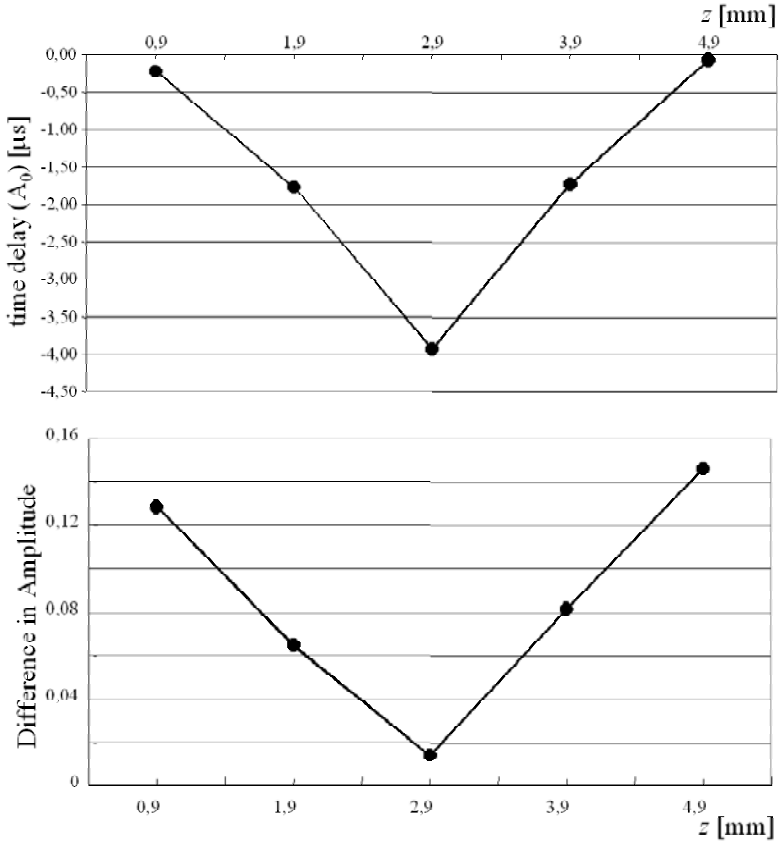

Figure 3.16. Dependence on the z-position of the single delamination. Time delay (upper plot) and difference in amplitude (lower plot) between the reference and the damaged case. (We have considered the out-of-plane v component of the displacement for the A_0 mode).

stack of delaminations can be observed, particularly in the first plot.

A quantitative evaluation of the effect of the damage can be very clearly evinced from Fig. 3.18, which displays the signal at the receiver. Here, besides the phase shift, we notice a much stronger decrease in the amplitude, due to the large number of delaminations in the stack.

3.2.4 Geometrically complex structures

Many of the fundamental aerospace structures include panels, sometimes of varying thickness, and reinforcing elements. The junctions between the

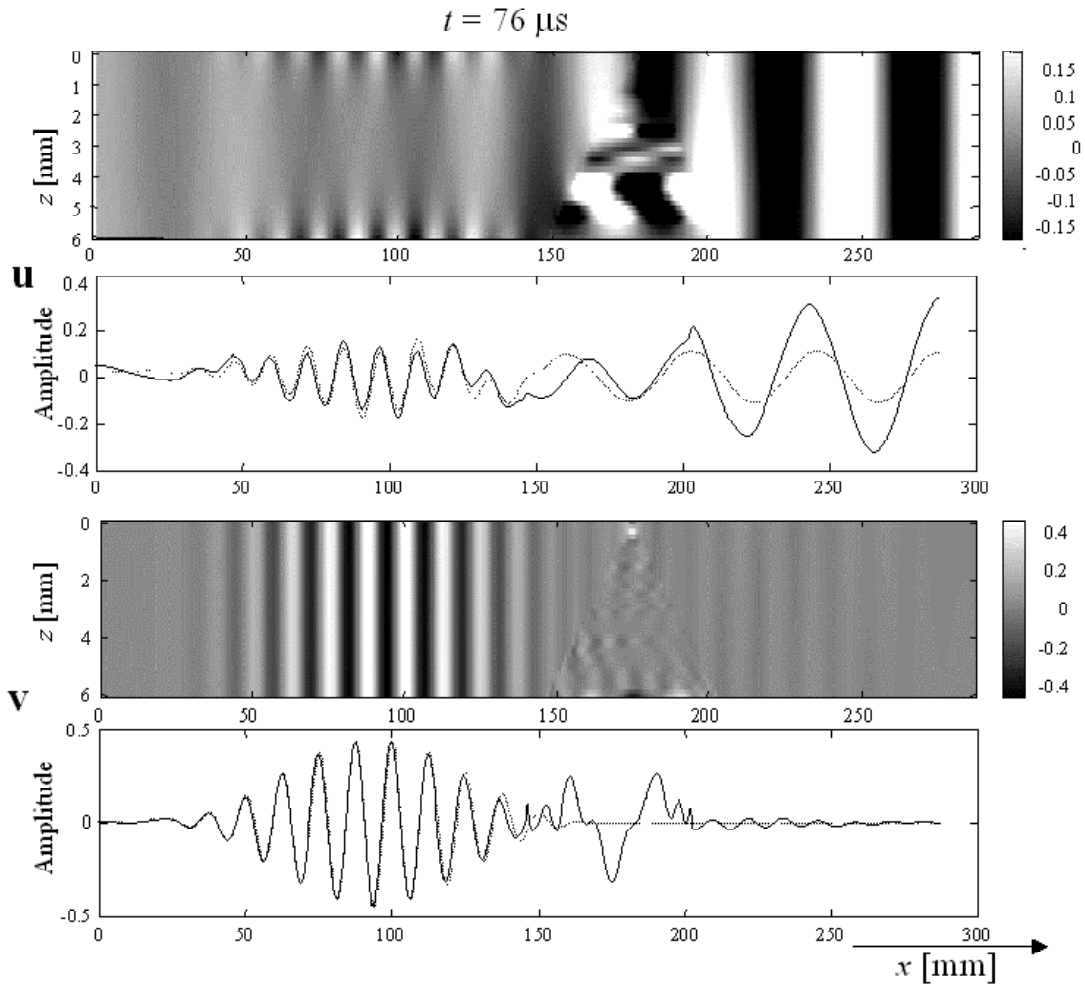

Figure 3.17. Snapshots at time $t = 76$ μs for a 6- mm-thick CFRP sample flawed by a cone-shaped stack of delaminations. The first plot represents the in-plane (u) component of the displacement; the second plot shows a section of the upper plot (continuous line) and the respective unflawed case (dotted line). The last two plots refer to the out-of plane v component of the displacement.

reinforcing elements and the panels are very important in evaluating the applicability of ultrasonic techniques to practical structures. Simulations may provide an insight into the interaction between LW's and these basic structures.

A detailed analysis of the results of our simulations in these kinds of

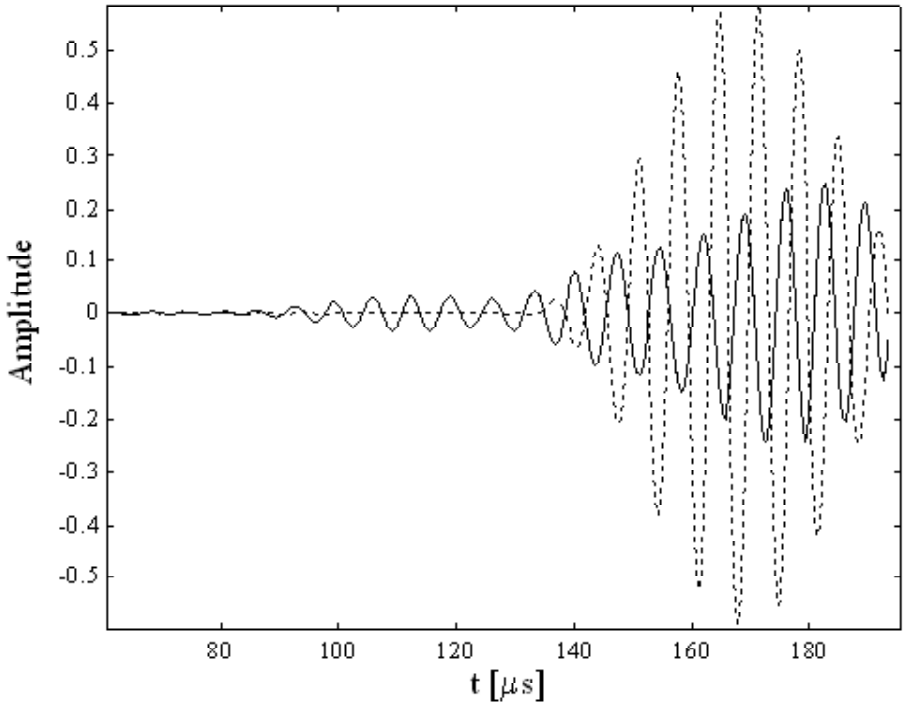

Figure 3.18. Signal collected at the receiver in a 6- mm-thick CFRP plate with a cone-shaped stack of delaminations.

structures is beyond the scope of this dissertation. I limit myself to present in Fig. 3.19 two examples of LW propagation in a T-junction stringer and a Y-junction stringer, respectively. As in the previous figures there is a wealth of propagation mechanisms, due to the discontinuous structure of the specimens, which can be exploited for the purpose of quantitative NDE.

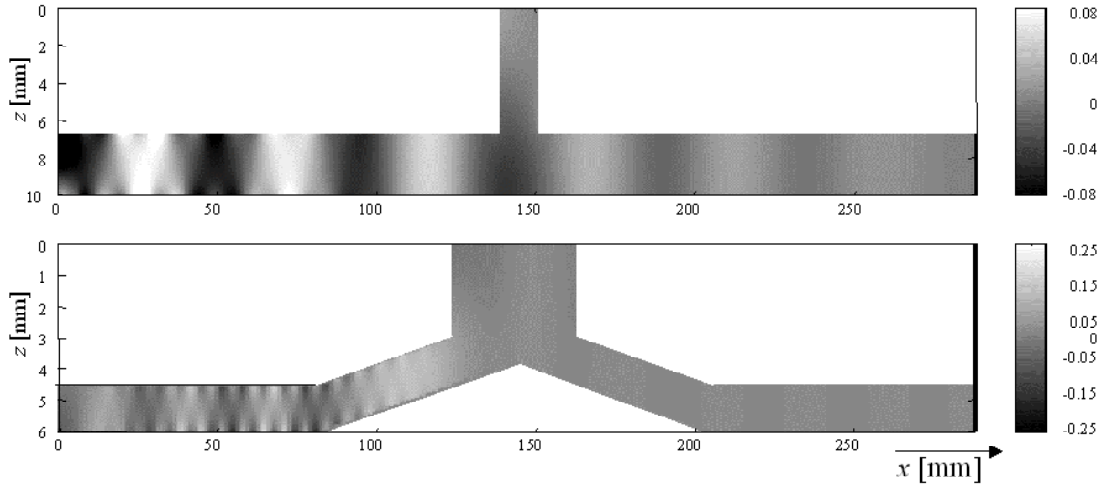

Figure 3.19. Upper plot:T-junction. Lower plot: Y-junction stringer. Snapshots of the in-plane component of the displacement.

Chapter 4

Nonlinear mesoscopic elasticity

4.1 Introduction

In Chapter 1 I have mentioned that among the various NDE techniques, acoustic methods [24] are perhaps the most frequently used. Recent advances in modern material technology require the development of NDE techniques that quantify micro-scale damages in a variety of materials, both during their production and life cycle. Ultrasonic waves interact with interface boundaries, grain interstices, pores, inclusions, cracks, etc. and gather substantial information about the details of the geometry and physical properties of the insonified medium.

In the last decade, numerous studies of a diverse class of materials such as earth materials, cement products, concrete, composites, etc. have shown that their elastic nonlinear behavior is significantly different from the classical nonlinear behavior found in "ordinary" materials, such as glasses, single crystals, numerous metals and others [16, 25, 26]. Despite their very different structural and chemical properties, these materials share the same nonlinear elastic behavior that can be observed in both quasi-static and dynamic experiments. In the following we shall say that these materials display "**nonclassical**" nonlinearity, while the "ordinary" materials, which obey the traditional nonlinear theory of Landau [15, 27] shall be called "**classical**" nonlinear.

The fundamental characteristics of nonclassical material behavior in quasi-static experiments is the appearance of stress-strain hysteresis and discrete memory [28]. Differences between nonclassical and classical nonlinear dynamic behavior include: a downshift of the resonance frequency, proportional to the resonance amplitude in the nonclassical case versus a quadratic amplitude dependence in the classical case; nonlinear attenuation versus amplitude independent attenuation; quadratic amplitude dependence of the third harmonic versus cubic in the classical case, respectively. [25] Another striking feature observed in the nonclassical nonlinear dynamic response of nonclassical materials is "**slow dynamics**", i.e., the slow recovery of the linear material properties (wave-speed and attenuation) after a sample has been subjected to a force[29, 30].

Nonclassical nonlinear effects are believed to be due to the presence of soft regions in hard materials (e.g. microcracks, flat pores and soft bonding regions between grains in a granular material). They have been successfully reproduced by a model of Guyer and McCall [31], based on a Preisach-Mayergoiz (PM) space representation, in analogy with the treatment of magnetic hysteresis. Such a model provides a simple phenomenological description of the complex elastic behavior of an elementary elastic unit in the composition of an arbitrary material. Each unit is described by an elementary constitutive law that accounts for effects such as nonlinearity, hysteresis and end-point memory. The collection of all units, each of them with their particular constitutive relations, yields the so called "**PM-space**", which characterizes the material specimen. Guyer and McCall used the PM-space to predict the static mechanical behavior of rocks in agreement with macroscopic observations. In the case of dynamic problems, Van Den Abeele et al. [32] used an analytical approximation of this model for homogeneous and isotropic nonlinear media to evaluate the influence of hysteresis on the propagation of longitudinal waves.

Analytical approaches must significantly simplify the problem and may not succeed in reproducing a whole set of observed phenomena. Application of numerical calculations can serve as an alternative for a more complete theoretical analysis, including the extension of a basic one-dimensional model to higher dimensions. Computer models based on a microscopic approach, such

as ab initio calculations and Molecular Dynamic techniques [33] are commonly used and allow, for instance, the understanding of atomic-scale details and their behavior under applied stresses [34]. However, such methods are not always practical because of the huge CPU time required, even for simulations over a small number of atoms. Therefore, a bridging of microscopic details towards a macroscopic description is extremely valuable.

In wave propagation applications, Delsanto et al. [5] proposed an approach for numerical simulations of macroscopic wave phenomena in complex heterogeneous media by introducing localized features at the mesoscopic level. The approach is based on the Local Interaction Simulation Approach (LISA) [2] in conjunction with a Spring Model [6]. A very important feature of LISA is, as its name implies, the capability of implementing at the local level even very complex mechanisms, which would be difficult to include in a Partial Differential Equation. In fact the method allows full freedom in the choice of interaction between the nodes which represent the boundaries of the material cells.

It is also possible, by splitting the nodes at the interfaces between different material components into "subnodes", each related to a different component, to include all kinds of microscopic-to-mesoscopic scale features. Recently, the PM-space micromodel suggested by Guyer and McCall was implemented numerically in the LISA framework to simulate the influence of the local nonlinear elastic properties on the one-dimensional dynamic wave propagation in nonclassical materials [35]. To my knowledge, this is the only study that explicitly incorporates the phenomenological PM-model in a macroscopic simulation of dynamic nonlinearity and hysteresis.

One of the drawbacks of numerical simulations is the difficulty of insuring the convergence and stability of the solutions. In this work, I propose a modification of the micromechanical properties of the individual units suggested by Guyer and McCall providing both a more physical description of the elasticity of the bond system, and a more stable numerical treatment.

In Sec. 4.2.1, I define for each unit the non-analytical constitutive law provided by the model and to be used as input for the LISA simulation. The main difference with the original micromodel of Guyer and McCall is that the units, which represent the interstices between grains, are also elastic and

therefore are not restricted to only two strain states ("open" and "closed"). In Sec. 4.2.2, a generalization of the spring model [6] is introduced for the simulation of the propagation of ultrasonic waves in classical materials, with both rigid and non rigid interfaces. The approach is then extended to the treatment of nonclassical nonlinearities.

In order to illustrate the applicability of the model, we focus our attention on simulations of a resonant bar experiment (Sec. 4.3) and show that our model is capable of reproducing all of the observed "nonclassical" nonlinear features.

4.2 Constitutive relations

Let us consider a bar of a multigrained material, as shown in Fig. 4.1a. For simplicity, we assume that all grains are homogeneous, aligned and that their centers are separated by an equal length L when no pressure is applied to the bar. Likewise we assume that, initially, all the interstices between grains have the same length $\delta^{(0)} \ll L$. The bar may then be represented by the 1-D lattice sketched in Fig. 4.1b: a sequence of elastic portions separated by interstice regions. The latter can be thought of as the bond system between the grains, i.e. grain contact areas, microcracks, cement paste, etc. In the following we will refer to the combination of elastic grain and interstice region as a lattice cell.

In the P-M space model[31], the interstice regions can exist only in two states: **open** or **closed**. In the open state the interstice has a length δ_o. When the pressure on the interstice increases, it will behaves rigidly and remains at its length δ_o up to a certain pressure P_c. At this pressure level, the interstice closes immediately (infinitely soft elasticity for an infinitesimal short time) and takes on the length δ_c ($\leq \delta_o$). Upon further increase of pressure, the interstice continues to behave rigid, this time with length δ_c. When decreasing the pressure, the interstice remains at its length δ_c down to a pressure level P_o ($\leq P_c$), where it instantaneously opens, and remains at a length δ_o upon further decrease of the pressure. The grains are considered to be purely elastic, represented by a modulus K_g. The corresponding stress-strain relations are shown in Fig. 4.2 (we consider stain ε to be positive if

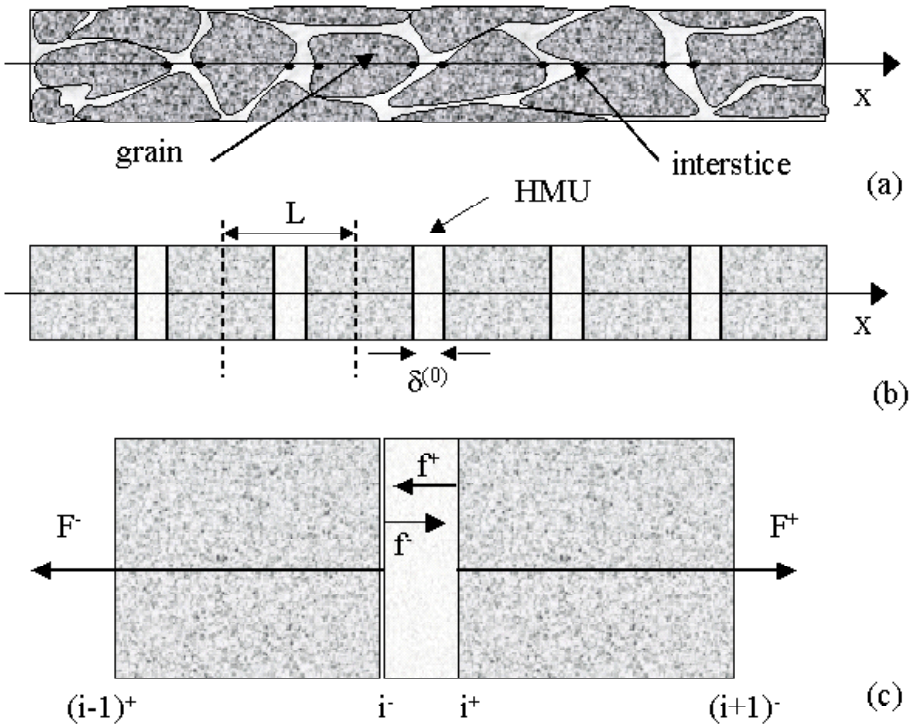

Figure 4.1. Schematic representation of: (a) a multigrained (micro-inhomogeneous) material; (b) a one-dimensional discrete version of micro-inhomogeneous medium; c) representation of the forces acting on the two subnodes delimiting an interstice.

the length is decreasing, and pressure is considered positive in compression, negative in tension).

It is important to note that the pairs (P_o,P_c) may have different values for each interstice, thus defining the PM-space. Even though an elastic unit and an interstice element are sequential in space, their combined elastic response has to be considered as the result of a parallel interaction. The residual modulus of a lattice cell K_{cell} must be calculated as follows:

$$\frac{1}{K_{cell}} = \frac{1}{K_g} + \frac{1}{K_I}$$

where K_I is the interstice modulus, which is infinity (rigid behavior) except at P_o and P_c. For completeness, we also illustrate in Fig. 4.2 the elastic response of a single lattice cell, both for $P_o \neq P_c$ (hysteretic jump

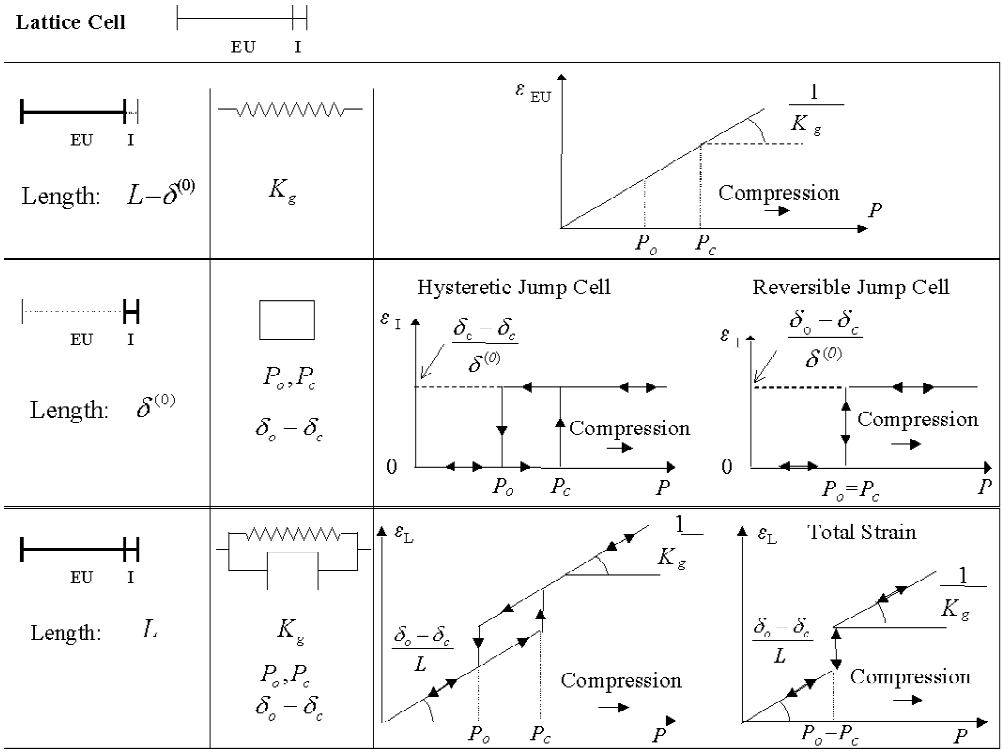

$$\varepsilon_{EU} = \frac{P}{K_g} \qquad \varepsilon_I = \begin{cases} 0 & \text{if } (P < P_c \text{ and } P \text{ increasing}) \text{ or } (P < P_o \text{ and } P \text{ decreasing}) \\ \dfrac{\delta_o - \delta_c}{\delta^{(0)}} & \text{if } (P > P_c \text{ and } P \text{ increasing}) \text{ or } (P > P_o \text{ and } P \text{ decreasing}) \end{cases}$$

$$\varepsilon_L - \frac{L-\delta^{(0)}}{L}\varepsilon_{EU} + \frac{\delta^{(0)}}{L}\varepsilon_I - \frac{L-\delta^{(0)}}{L}\frac{P}{K_g} + \begin{cases} 0 & \text{if } (P < P_c \text{ and } P \text{ increasing}) \text{ or } (P < P_o \text{ and } P \text{ decreasing}) \\ \dfrac{\delta_o - \delta_c}{L} & \text{if } (P > P_c \text{ and } P \text{ increasing}) \text{ or } (P > P_o \text{ and } P \text{ decreasing}) \end{cases}$$

$$\text{and thus:} \quad \varepsilon_L \approx \frac{P}{K_g} + \begin{cases} 0 & \text{if } (P < P_c \text{ and } P \text{ increasing}) \text{ or } (P < P_o \text{ and } P \text{ decreasing}) \\ \dfrac{\delta_o - \delta_c}{L} & \text{if } (P > P_c \text{ and } P \text{ increasing}) \text{ or } (P > P_o \text{ and } P \text{ decreasing}) \end{cases}$$

Figure 4.2. The micro-model of Guyer and McCall illustrating the stress-strain behavior of a typical lattice cell composed of an elastic unit and a non-classical interstice. The grains are purely elastic, the interstices display jump and hysteresis phenomena. The total strain on a lattice cell can be calculated by a series interaction. A statistical ensemble of such cells represents a micro-inhomogeneous material.

cell) and for $P_o = P_c$ (reversible jump cell). Apart from two geometric parameters (L,$\delta^{(0)}$), lattice cells in this model are thus represented by four "elastic" parameters: K_g,P_o,P_c, and $\delta_o - \delta_c$.

For numerical simulations, the appearance of jumps in the state relation may cause problems of convergence and stability. Also, from a physical point of view, discontinuities are unrealistic. Ideally, it would be most satisfactory to describe the elastic behavior by smooth analytic functions. As an example, the expressions:

$$\varepsilon = \begin{cases} \frac{P}{K_g} + \frac{(P+P_c-\ln(\cosh(P-P_c)))}{2K_l} + \overline{\varepsilon}\left(1+\tanh\frac{P-P_c}{\chi}\right) \\ \qquad\qquad \text{if } P \text{ increases} \\ \frac{P}{K_g} + \frac{(P+P_o-\ln(\cosh(P-P_o)))}{2K_l} + \\ \qquad + \left(\overline{\varepsilon} + \frac{P_c-P_o}{2K_l}\right)\left(1+\tanh\frac{P-P_o}{\chi}\right) \\ \qquad\qquad \text{if } P \text{ decreases} \end{cases}$$

yield the elastic stress-strain behavior of a lattice cell illustrated in Fig. 4.3.

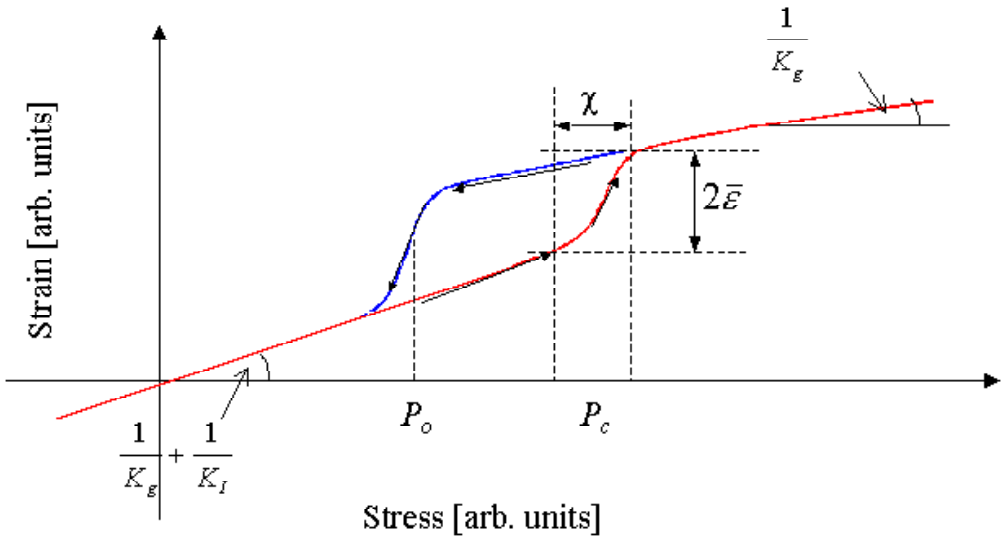

Figure 4.3. A continuous micro-model illustrating the stress-strain behavior of a single lattice cell characterized by a set of six "elastic" parameters: K_g, K_I, P_o, P_c, $\bar{\varepsilon}$ and χ. The micro-model of Guyer and McCall corresponds to the case when $\chi = 0$ and $K_I \to \infty$.

Here, a total of six "elastic" parameters are involved: K_g,K_I,P_o,P_c,$\overline{\varepsilon}$, and χ. K_I introduces a difference in elasticity modulus before and after the hysteretic open-closure pressure range; $\overline{\varepsilon}$ reflects the magnitude of the jump in strain at P_c and χ takes into account the smoothness of the transitions at P_c and P_o. The P-M space of Guyer and McCall can be reproduced in the limit of $K_l \to \infty$ and $\chi = 0$, i.e. when there is no change in elasticity modulus before and after closure, and the closing and opening are instantaneous in pressure.

However, since we are treating the bond system as soft inclusions, it is reasonable to assume that the modulus of a lattice cell alters when the mesoscopic features change states. Therefore, it seems appropriate to retain the interstice softness parameter K_l at a value different from infinity. In order to limit the number of free parameter values to four, as in the original P-M space model, we put $K_I = \chi = 0$. In doing so, we have adjusted the micromechanical properties of the bond elements as follows: Instead of opening and closing discontinuously in pressure, the interstice element behaves linearly elastic, with modulus $\overline{K}_I = \frac{\delta^{(0)}}{L} K_I$, up to a certain pressure P_c. At that pressure level, the element becomes rigid (infinite modulus), and it remains rigid for all pressures above. When decreasing the pressure, the interstice remains at a fixed length down to a pressure level P_o, where it instantaneously opens and continues afterwards to increase its length according to Hooke's law

$$\varepsilon_I = \frac{\delta^{(0)} - \delta}{\delta^{(0)}} = \frac{P}{\overline{K}_I}. \tag{4.1}$$

The sudden decrease in strain (increase in length) of the lattice cell at P_o amounts to $\frac{P_c - P_o}{K_I}$. The corresponding stress-strain behavior of the elastic unit, the interstice element, and the total lattice cell are shown in Fig. 4.4. As in the case of the original PM-space model, the micromechanical behavior can be described by piecewise linear functions. If $P_o = P_c$, we talk of a Reversible Mesoscopic Unit (RMU). If P_o differs from P_c, we use the term Hysteretic Mesoscopic Unit (HMU).

Our new representation has the advantage of having eliminated one of

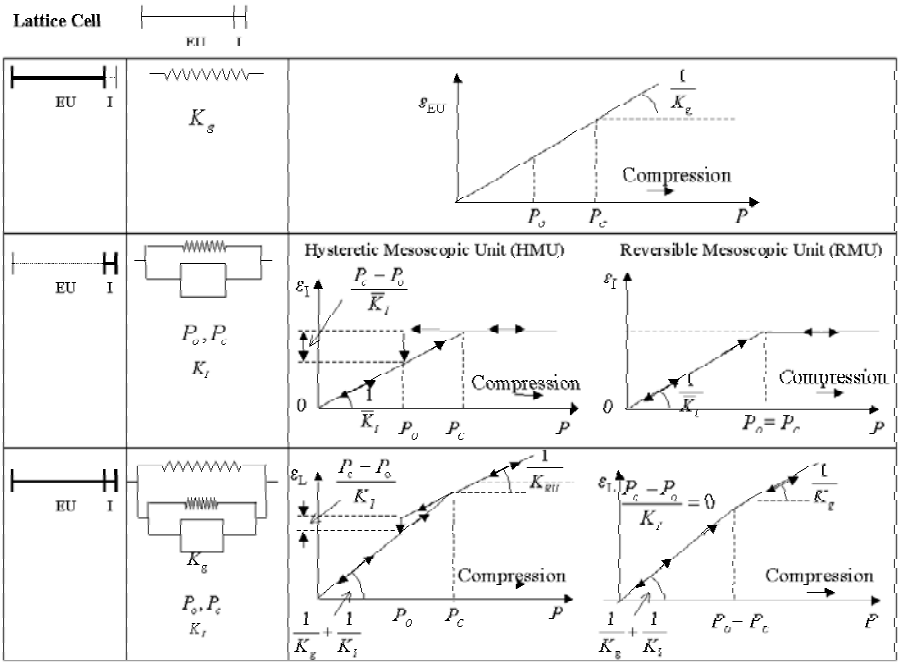

$$\varepsilon_{EU} = \frac{P}{K_g} \qquad \varepsilon_I = \begin{cases} \dfrac{P}{K_I} & \text{if } (P < P_c \text{ and } P \text{ increasing}) \text{ or } (P < P_0 \text{ and } P \text{ decreasing}) \\ \dfrac{P_c}{K_I} & \text{if } (P > P_c \text{ and } P \text{ increasing}) \text{ or } (P > P_0 \text{ and } P \text{ decreasing}) \end{cases}$$

$$\varepsilon_L = \frac{L - \delta^{(\circ)}}{L}\varepsilon_{EU} + \frac{\delta^{(\circ)}}{L}\varepsilon_I = \frac{L - \delta^{(\circ)}}{L}\frac{P}{K_g} + \begin{cases} \dfrac{\delta^{(\circ)}}{L}\dfrac{P}{K_I} = \dfrac{P}{K_I} & \text{if } (P < P_c \text{ and } P \text{ increasing}) \\ & \text{or } (P < P_0 \text{ and } P \text{ decreasing}) \\ \dfrac{\delta^{(\circ)}}{L}\dfrac{P_c}{K_I} = \dfrac{P_c}{K_I} & \text{if } (P > P_c \text{ and } P \text{ increasing}) \\ & \text{or } (P > P_0 \text{ and } P \text{ decreasing}) \end{cases}$$

$$\text{and thus: } \varepsilon_L \approx \frac{P}{K_g} + \begin{cases} \dfrac{P}{K_I} & \text{if } (P < P_c \text{ and } P \text{ increasing}) \text{ or } (P < P_0 \text{ and } P \text{ decreasing}) \\ \dfrac{P_c}{K_I} & \text{if } (P > P_c \text{ and } P \text{ increasing}) \text{ or } (P > P_0 \text{ and } P \text{ decreasing}) \end{cases}$$

Figure 4.4. The currently used micro-model illustrating the stress-strain behavior of a typical lattice cell composed of a purely elastic unit and a non-classical interstice displaying both elasticity, as well as jump and hysteresis phenomena. The total strain on a lattice cell can be calculated by a series interaction. This micro-model can be found from the general continuous model (Fig. 4.3) by setting both $\bar{\varepsilon}$ and χ equal to zero.

the discontinuities in the stress-strain behavior. This is important for the stability and convergence of the simulations. In the following Section, we implement this type of mesoscopic elastic behavior in the framework of the Local Interaction Simulation Approach (LISA). First we consider the case of "classical phase" materials with completely rigid bonds, then we introduce linearly elastic bonds, and finally we implement the case of bonds with the assumed nonlinear elasticity to describe the macroscopic dynamic behavior of "nonclassical " materials.

4.3 Application of the LISA model to NME materials

As shown in Fig. 4.1, each lattice cell consists of an elastic portion (grain) and an interstice element (bond). According to our model, the latter is responsible for the mesoscopic hysteretic response. In order to describe the interstice region between two grains, each grid node point i is split into two sub-nodes $i^{\pm}$ (see Fig. 4.1c). Since in dynamical experiments the contribution of classical nonlinearity is generally negligible, we assume that the grains are linearly elastic. Associated with each sub-node is a length $L_n = L/2$ (i.e. of half a grain) and a mass $m_n = \rho L_n$, where ρ is the mass density per unit length. The interstices are considered to have zero mass (because $\delta^{(0)}$ is assumed to be very small). We call the combination of two sub-nodes left and right of a grid node, with their lengths and masses, a GBG-cell (grain-bond-grain). Depending on the elastic behavior of the grains and the bond, this cell can be linearly elastic, classical nonlinear or nonclassical nonlinear.

For the simulation of dynamic processes, we also consider a time discretization $t = 0,1,2,...$ with a constant time step τ. When referring to length δ, displacement u and forces F,f the first subscript always refers to the space discretization, whereas the second refers to the time discretization. starting with eq. 4.4, we will usually omit one or both indices when equal to the "current" values of i and/or t.

4.3.1 Classical Phase materials

Classical phase materials are elastic materials with a classical bond system, i.e., the elastic behavior of both grains and bonds is linear or classically nonlinear. A particular case is when all of the interstices behave rigidly, i.e. the length of each interstice remains constant:

$$\delta_{i,t} = u^{+}_{i,t} - u^{-}_{i,t} = const \qquad \forall T_0 \leq t \leq T_1 \tag{4.2}$$

This corresponds to the case of "perfect contact" in ref. [6]. However $\delta_{i,t}$ may also vary, provided the elastic modulus (i.e. the derivative of the stress with respect to the strain) is a continuous function of the applied stress.

To describe the general case, we assume that the following forces are acting on each sub-node (we use the convention that forces are positive when pointing to the positive x-direction):

1. an "external" elastic force $F^{\pm}_{i,t}$, due to the presence of an excitation of the bar at the interstice i at the time t. Neglecting, as mentioned, the classical nonlinear terms:

$$F^{\pm}_{i,t} = K_g \frac{u^{\mp}_{i\pm1,t} - u^{\pm}_{i,t}}{L} \tag{4.3}$$

where K_g is the stiffness of the grains and $u^{\pm}_{i,t}$ is the sub-node displacement.

1. a "dissipative" force $\mp\gamma\dot{u}$, which is required in the simulation of dynamic resonance experiments in order to obtain steady state solutions.

2. an "internal" force, which acts on the interstice to keep the two sub-nodes together and transmit the external excitation through the bar (see ref. [6]). Since the interstice itself has no mass: $f^{+}_{i,t} = -f^{-}_{i,t} = f_{i,t}$.

3. an elastic "restoring" force: $\Im^{+}_{i,t} = \mp K_l \left(\delta_{i,t} - \delta^{(0)}_i\right)$, where $\delta^{(0)}_i$ is the rest length of interstice i when no forces are present.

   The equation of motion for the two sub-nodes is then:

$$\rho L_n \ddot{u}^{\pm}_{i,t} = F \mp \gamma \dot{u}^{\pm} + f^{\pm} + \Im^{\pm} \tag{4.4}$$

By subtracting and summing these equations, we obtain:

$$\rho L_n \ddot{\delta} = p - \gamma \dot{\delta} + 2f + \Im^{+} - \Im^{-} \tag{4.5}$$

and

$$\rho L_n \ddot{y} = F - \gamma \dot{y} \tag{4.6}$$

where

$$\delta = u^{+} - u^{-} \tag{4.7}$$

$$p = F^{+} - F^{-} \tag{4.8}$$

$$y = \frac{u^{+} + u^{-}}{2} \tag{4.9}$$

$$F = \frac{F^{+} + F^{-}}{2} \tag{4.10}$$

Rigid interstice case

In a time interval $(t,t+1)$ in which the interstice remains rigid, i.e. $\delta_{t+1} = \delta_t$, it follows:

$$\dot{\delta} \approx \frac{\delta_{t+1} - \delta_{t-1}}{2\tau} = \frac{\delta_t - \delta_{t-1}}{2\tau} = \frac{\Delta\delta_{t-1}}{2\tau} \tag{4.11}$$

$$\ddot{\delta} \approx \frac{\delta_{t+1} - 2\delta_t + \delta_{t-1}}{\tau^2} = -\frac{\Delta\delta_{t-1}}{\tau^2} \tag{4.12}$$

where we have applied the usual first order finite difference formalism together with the definition of the forward difference operator

$$\Delta y_k = y_{k+1} - y_k.$$

Substituting eqs. 4.11, 4.12 and eq. 4.5 and from the definitions of $\Im^{\pm}$, it follows

$$f = -\frac{p}{2} - \frac{a}{2}\Delta\delta_{t-1} + K_I\left(\delta - \delta^{(0)}\right) \tag{4.13}$$

where

$$a = \frac{1}{2\tau}\left(\frac{2\rho L_n}{\tau} - \gamma\right). \tag{4.14}$$

Note that if δ never changes (permanently rigid interface), $\Delta\delta_{t-1} = 0$ and $\delta = \delta^{(0)}$ at all times, and we obtain:

$$f = -\frac{p}{2} \tag{4.15}$$

as in ref. [2]. In this case, $u^+ = u^-$ at each time.

Classical interstice case

When the interstice is not rigid, the arrival of an external excitation may change its length. Then, at least locally, we must assume that the material is undergoing a change. Accordingly, we modify eq. 4.13 by multiplying the three terms in the r.h.s. by three bond "quality" parameters q,q' and q'' (less or equal to unity), which allow us to specify the quality of the interface bond at the time t:

$$f = -q\frac{p}{2} - q'\frac{a}{2}\Delta\delta_{t-1} + q''\overline{K}_l\left(\delta - \delta^{(0)}\right) \tag{4.16}$$

In the general case of a "classical" interstice, q,q' and q'' may depend on the stress in a continuous and reversible way. The rigid interstice phase is recovered by placing all values equal to unity.

Substituting eq. 4.16 into eq. 4.5), we obtain:

$$\rho L_n\ddot{\delta} = rp - \gamma\dot{\delta} - q'a\Delta\delta_{t-1} - 2r''\overline{K}_l\left(\delta - \delta^{(0)}\right) \tag{4.17}$$

where $r = 1 - q$,$r'' = 1 - q''$. eq.. 4.6 remains unaffected because it does not involve the internal forces.

Following eq. 4.17, the overall elastic properties of the GBG-cells are defined by an effective elastic constant, which is a function of the elastic

constants of the grain and the bond, and of the (instantaneous) values of the bond quality parameters:

$$K_{eff} = \Phi\left(K_g, K_l, q, q', q''\right) \tag{4.18}$$

Since $u^{\pm} = y \pm \frac{\delta}{2}$ we obtain from eqs. 4.6 and 4.17:

$$\begin{aligned} 2\rho L_n^{\pm}\ddot{u}^{\pm} &= (1+r)\,F^{\pm} + (1-r)\,F^{\mp} - 2\gamma\dot{u}^{\pm} \\ &\quad \mp q' a\left(\Delta u_{t-1}^{+} - \Delta u_{t-1}^{-}\right) \\ &\quad \mp 2r'' K_l\left(u^{+} - u^{-} - \delta^{(0)}\right) \end{aligned} \tag{4.19}$$

From eqs. 4.3, 4.14, and 4.19, and by assuming that L and τ are chosen in order to assure optimal convergence:

$$\frac{2L_n}{\tau} = \sqrt{\frac{K_g}{\rho}} \tag{4.20}$$

it follows:

$$\begin{aligned} B\ddot{u}_{t+1}^{\pm} &= (1+r)\,u_{i\pm 1,t}^{\mp} + (1-r)\,u_{i\mp 1,t}^{\pm} - 2Au_{i,t-1}^{\pm} + \\ &\quad + q' A\left(u_{t-1}^{\pm} - u_{t-1}^{\mp}\right) + E(u^{\pm} - u^{\mp}) \\ &\quad \pm \frac{2K_l r''}{C}\delta^{(0)} \end{aligned} \tag{4.21}$$

where

$$C = \frac{2L_n\rho}{\tau^2} = \frac{K_g}{2L_n}; B = 1 + \frac{\gamma}{C\tau} \tag{4.22}$$

$$A = \frac{a}{C} = 1 - \frac{B}{2} \tag{4.23}$$

and

$$E = 1 - r - q' A - \frac{2K_l r''}{C}. \tag{4.24}$$

4.3.2 Non-classical phase materials

In a classical phase material, the parameters q,q' and q'' at each grid point are smooth single valued functions of the stress. In a nonclassical material, the internal structure may vary discontinuously and non-uniquely as a function of the applied stress. The discontinuous or non-unique stress dependence may be due to various physical mechanisms, e.g. a redistribution of dislocations, crack activation (opening or closing) or frictional forces (jerks). In the case of mesoscopic materials it is reasonable to assume that these changes affect only the interstice region. The effects at the mesoscopic scale may be conveniently modeled by introducing a more complex dependence of the bond quality parameters q,q' and q'' on the applied pressure. As a consequence, the overall elastic properties of the GBG-cell are defined by an effective elastic constant which is a function of the time-average of the bond quality parameters:

$$K_{eff} = \Phi\left(K_{EU},K_l, \langle q\rangle_t, \langle q'\rangle_t, \langle q''\rangle_t\right) \tag{4.25}$$

To describe the dependence of the bond quality parameters on the externally applied driving pressure in a nonclassical phase, we apply a PM space approach[31], which is the natural generalization of the one described in sec. 5.2. We assign a pair of pressure parameters P_o and P_c to each GBG-cell ($P_o \leq P_c$). When the applied pressure reaches the value P_c, we allow the bond-quality parameters to switch from their initial values to unity, meaning that the bond becomes rigid for $P > P_c$. Conversely, when P decreases below P_o, the bond-quality parameters are switched to a value less than unity. The protocol for the bond quality parameter q as a function of the applied pressure P is schematized in Fig. 4.5. Since q' affects only the wave attenuation, which is not relevant in the present context, we keep for simplicity $q' = 1$ at all times. Likewise we set $q'' \equiv q$ at all pressures. Other choices of protocol are, of course, possible and might be found more suitable in general or in particular situations.

In the above described protocol, the specimen is represented as a sequence of GBG-cells, each defined by a pair of activation pressures and by an initial bond state configuration. If $P \geq P_c$ or $P \leq P_o$, there is only one possible state, rigid or elastic, respectively. In the pressure range $P_o < P < P_c$

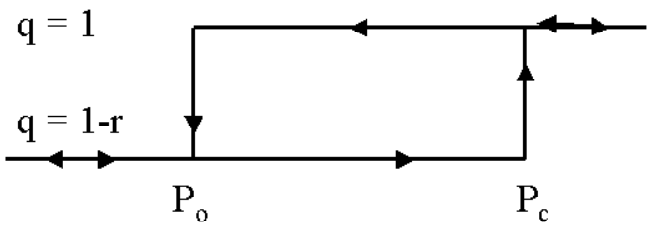

Figure 4.5. Representation of the protocol for the dependence of the bond quality factor q on the applied pressure.

two different states are possible, depending on the activation history of the GBG. The distribution of the pair of values (P_o,P_c), represented by the density $\rho_{NC}(P_o,P_c)$ of nonclassical GBG-cells (hysteretic and reversible mesoscopic units), can be obtained by inversion of quasi-static stress-strain measurements [36, 37].

The initial q-distribution (at $t = 0$) is strongly affected by the previous activation history of the specimen. In the following the specimen is assumed to be, at the time $t = 0$, completely relaxed, i.e. having been kept at atmospheric pressure ($P = 0$ after proper rescaling) and constant temperature for a sufficiently large time interval. Therefore, we consider the following initial conditions:

$$\begin{aligned} q &= 1 \qquad \text{if} \qquad P_o < 0 \\ q &= 1 - r \qquad \text{if} \qquad P_o > 0 \end{aligned} \tag{4.26}$$

Once the initial configuration is set and the external forcing protocol properly defined, the iteration equations 4.21 allow to follow the temporal evolution of the system.

4.4 Simulations of nonlinear resonant bar experiments

In the following we focus our attention on a resonant bar experiment performed on a typical material exhibiting nonclassical nonlinearity [16]. We assume that a rod-shaped specimen is equipped with a transducer generating monochromatic waves of excitation amplitude A_d at a varying drive frequency f_d attached at one end and with an accelerometer attached to the other end. At a given excitation level A_d, the frequency f_d is swept through the fundamental resonance mode f_o of the specimen and the time averaged acceleration amplitude A_r (in stationary conditions) is recorded. This procedure of resonance curve tracking is repeated for several different levels of excitation.

In the simulation approach, each mesoscopic unit (HMU or RMU) corresponds to a point in the PM space (see Fig. 4.6a). The dark and light gray areas in the plot correspond to initially soft and rigid interstices, respectively. In the stationary state of a resonance, the actual pressure P for each HMU/RMU oscillates between a minimum and a maximum pressure (P_{min} and P_{max}, respectively), depending on the external excitation level and on its location in the bar (see Fig. 4.6b). If the HMU/RMU is situated within the activation triangle (the PM-space area bounded by the diagonal $P_o = P_c$ and the lines $P_o = P_{min}$ and $P_c = P_{max}$), the nonlinear properties are activated by the forcing (white area in the plot). As a consequence, the bond will change during the excitation process between rigid and soft. If we assume that the density $\rho_{NC}(P_o,P_c)$ in PM-space is locally uniform and we increase the forcing by a factor two, we expect the number of activated units to increase by a factor of four. This implies that the strain is affected in a quadratic manner and, as a consequence, the dynamic modulus of the specimen changes approximately proportionally to the resonance amplitude. Likewise, we expect that the hysteretic contribution from the activated HMU's to the relative energy loss per cycle

$$2\xi = \frac{1}{Q} = \frac{\Delta E}{\overline{E}}, \tag{4.27}$$

induces an increase in the effective modal damping ratio ξ that is, to a good

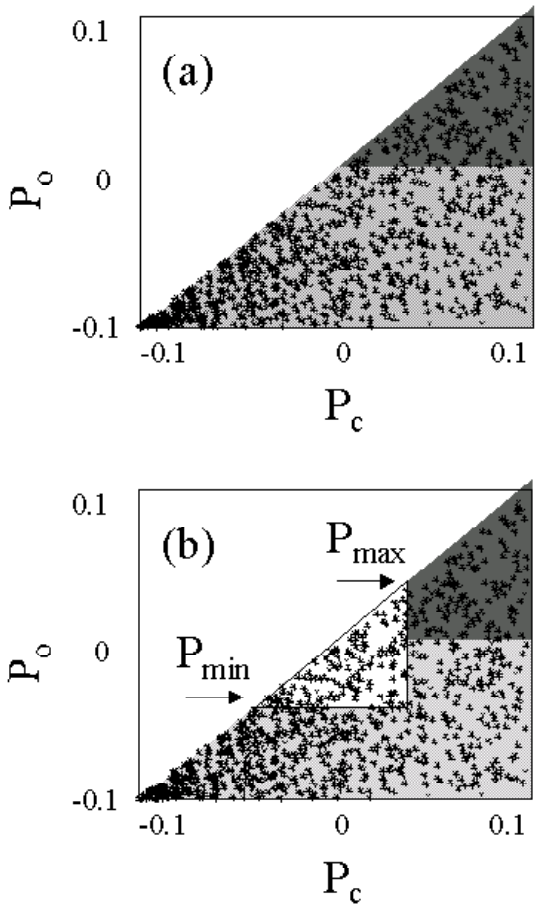

Figure 4.6. PM-space representation. Each dot represent one HMU or RMU. (a) specimen in the initial condition at zero pressure.Units in the dark gray, and light gray areas are initially soft or rigid, respectively.; (b) specimen under an external sinusoidal driving between p_{min} and p_{max}.Units in the dark gray, light gray and white areas are permanently soft, permanently rigid and active, respectively.

approximation, proportional to the resonance amplitude. In eq. 4.27, ΔE is the energy loss per strain cycle, and $\overline{E}$ the average energy during a cycle.

Figure 4.7 illustrates a typical numerical simulation of the resonant bar experiment. The time averaged acceleration amplitude on the free edge is plotted vs. frequency for several driving amplitudes in Fig. 4.7a. From the plot (using polynomial interpolation), one can determine the resonance frequency and its amplitude. The width of the resonance curve is a measure

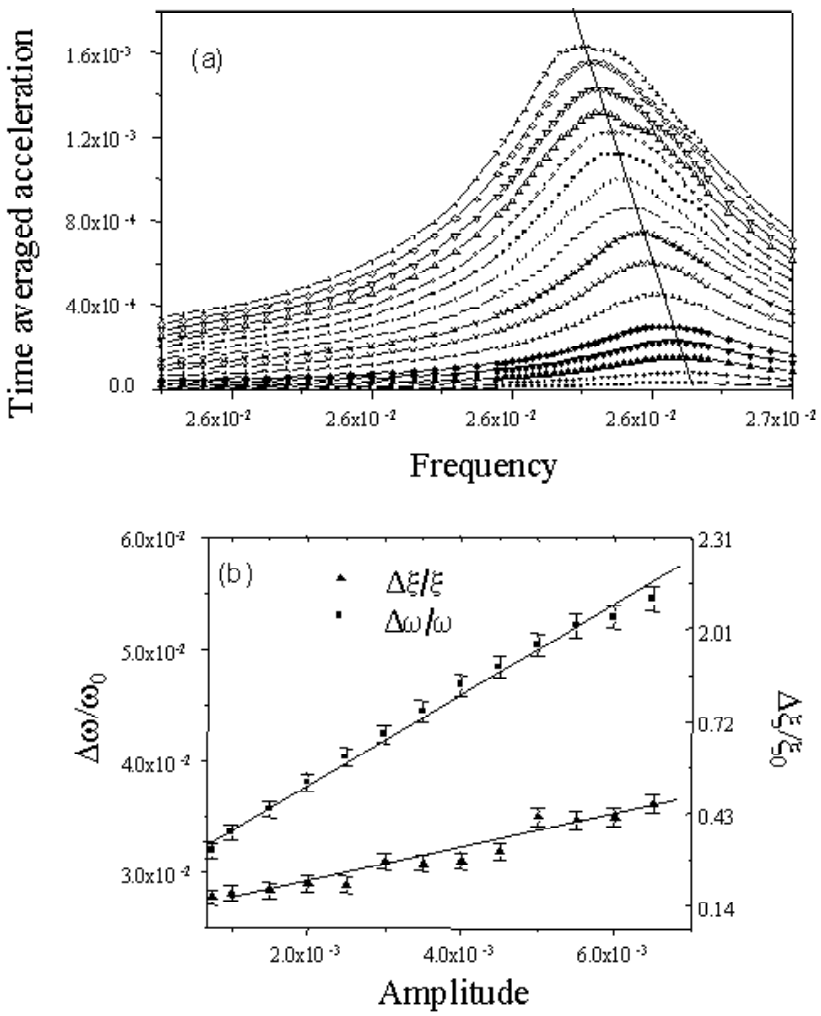

Figure 4.7. Result of a resonant dynamic experiment. (a) time averaged acceleration vs. frequency for different driving amplitudes. (b) normalized frequency shift and attenuation vs. the output wave amplitude at resonance.

of the attenuation. In the case of skewed resonance curves the attenuation can be obtained by means of the RTMF method proposed by Smith et al. [38]. The relative changes of frequency and attenuation vs. the resonance amplitude are shown in Figure 4.7b. They both display a linear dependence on the amplitude of the output acceleration in resonance.

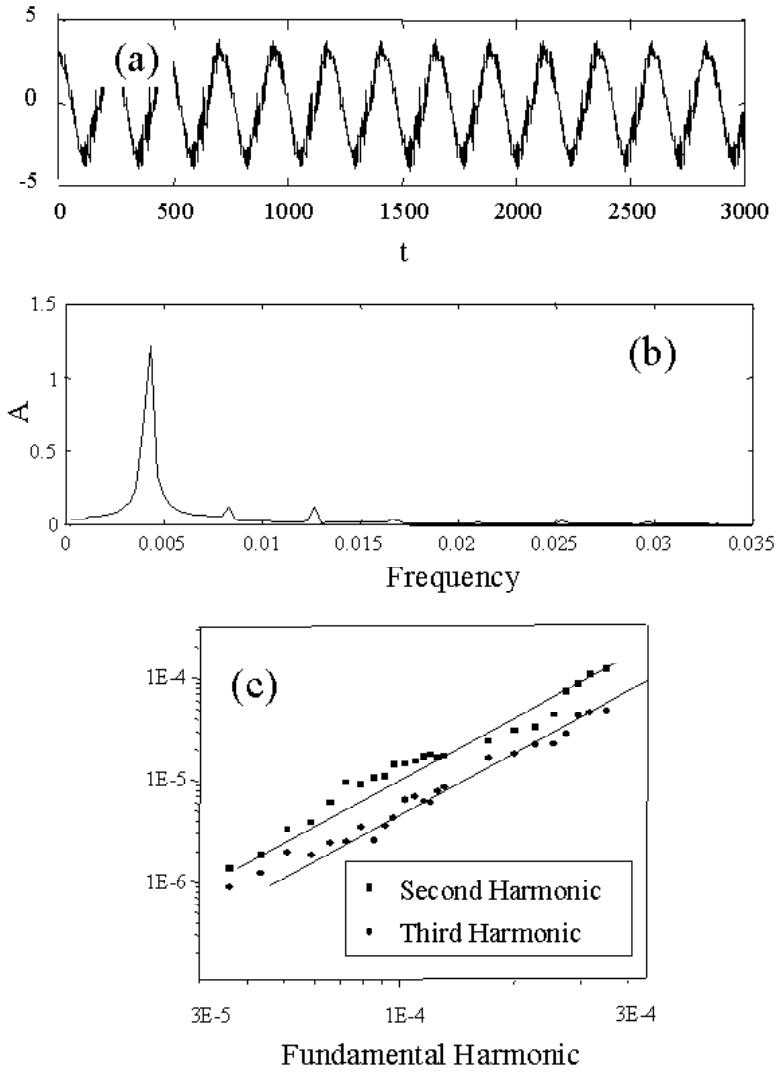

Figure 4.8. Generation of higher order harmonics. (a) temporal signal (acceleration vs. time); (b) Fast Fourier Transform of the signal; (c) amplitudes of the second and third harmonics vs. the fundamental.

The temporal signal in resonance is reported in Fig. 4.8a for a given driving amplitude. The signal (perfectly sinusoidal in the linear case or at very low driving amplitudes) is distorted due to the nonlinearity. The triangular shape is typical of hysteretic behavior in the system. The Fast Fourier Transform (FFT) of the signal is reported in Fig. 4.8b. As expected, higher order

harmonics (both even and odd) are generated. Note that the third harmonic is larger than the second, since both classical and nonclassical nonlinearities are responsible for its formation, while only classical nonlinearity contributes to the second harmonic. Finally, in Fig. 4.8c we analyze the dependence of the second and third order harmonics on the amplitude of the fundamental one in a log-log plot. Both curves have slope two, in agreement with experimental data. We recall that the expected slopes in the classical nonlinear case are two and three for the second and third harmonics, respectively.

References

[1] P. P. Delsanto, T. Whitcombe, H. H. Chaskelis and R. B. Mignogna, "Connection machine simulation of ultrasonic wave propagation in materials I: the one dimensional case", Wave Motion **15,** 65-80 (1992).

[2] P. P. Delsanto, R. S. Schechter, H. H. Chaskelis, R. B. Mignogna and R. Kline, "Connection machine simulation of ultrasonic wave propagation in materials II: the two dimensional case", WaveMotion **20,** 297-314 (1994).

[3] P. P. Delsanto, R. S. Schechter and R. B. Mignogna, Connection machine simulation of ultrasonic wave propagation in materials III: the three dimensional case, Wave Motion **26**, 329-339 (1997).

[4] R. S. Schechter, H. H. Chaskelis, R. B. Mignogna and P. P. Delsanto, "Real-time parallel computation and visualization of ultrasonic pulses in solids using the connection machine, Science **265**, 1188-92 (1994).

[5] P. P. Delsanto, R. B. Mignogna, R. S. Schechter and M. Scalerandi, Simulation of ultrasonic pulse propagation in complex media, in *New Perspectives on Problems in Classical and Quantum Physics*, ed.s P.P.Delsanto and A.W.Saenz, (Gordon Breach -1998), v.2 pp. 51-74.

[6] P.P. Delsanto, M. Scalerandi, "A Spring Model for the Simulation of Wave Propagation Across Imperfect Interfaces", J. Acoust. Soc. Am. **104** (5), 1-8 (1998).

[7] P. P. Delsanto, G. Perego, M. Scalerandi and D. Zoccolan, "Efficiency of Different Ultrasonic Surface Waves for Subsurface Flaws Detection",

Review of Progress in Quantitative Non Destructive Evaluation **18A** (Plenum Press, 1999), 127-133.

[8] P. P. Delsanto, N. K. Batra, R. B. Mignogna and M. Scalerandi, "Parallel Processing Simulations of the Propagation of Ultrasonic Waves through Material Interfaces", in Proceedings of 1998 IEEE Ultrasonic Symposium, Sendai, Japan 1998, 1129-1138.

[9] P.A.Johnson and R.A.Guyer, Physics Today, 30-36, (April 1999).

[10] Progress Reports of the "DAMASCOS" project No BE-97.4213, funded by the EC (1998-2000).

[11] J. L. Rose, *Ultrasonic Waves in Solid Media*, (Cambridge University Press, 1999).

[12] I. A. Viktorov, *Rayleigh and Lamb Waves*, (Plenum Press, New York, 1967).

[13] N. Guo and P. Cawley, J. Acoust. Soc. Am. **94**, 2240 (1993).

[14] V. Agostini, P.P. Delsanto, I. Genesio, "Simulation of Lamb wave propagation for the characterization of complex structures", submitted to IEEE Trans. on Ultras., Ferroel., and Freq. Control (2001).

[15] L.D.Landau, E.M.Lifshitz, *Theory of Elasticity*, (Pergamon, Oxford, 1986).

[16] R.A.Guyer, P.A.Johnson, Physics Today **52**, 30 (1999).

[17] M. Scalerandi, V. Agostini, P.P. Delsanto, K.Van Den Abeele, P.A.Johnson, "Local Interaction Simulation Approach to modelling nonclassical, nonlinear elastic behavior in solids", submitted to Physical Review Letters (2001).

[18] H.F. Pollard, *Sound Waves in Solids*, (Pion Limited, London, 1977).

[19] N. Bellomo and L. Preziosi, *Modelling Mathematical Methods and Scientific Computation,* (CRC Press, 1995).

[20] J. C. Strickwerda, *Finite Difference Schemes and Partial Differential Equations*, (Wadsworth-Brooks, 1989).

[21] T. Monnier 1999, private communication.

[22] V. Agostini, J.-C. Baboux, P.P. Delsanto, T. Monnier, D. Olivero, Application of Lamb Waves for the Characterization of Composite Plates, in "Non Destructive Characterization of Materials IX", ed.by R.E.Green (AIP proceedings, Melville, New York, 1999), 455-460.

[23] A. Chahbaz, V. Mustafa and D. Hay, Corrosion Detection in Aircraft Structures using Guided Lamb Waves", NDTnet, November 1996, v.1, No. 11.

[24] Y. Zheng, R. Maev, I. Solodov, "Non-linear acoustic applications for material characterization: A review," Can. J. Phys. Vol. **77**, 927-967 (1999).

[25] R.A.Guyer, J.A.Tencate, P.A.Johnson, Phys.Rev.Lett. **82**, 3280-3283 (1999).

[26] J.A.TenCate, K.E-A. Van Den Abeele, T.J.Shankland, P.A.Johnson, J.Acoust.Soc.Am. **99**, 3334-3345 (1996).

[27] K.Van den Abeele, J.Acoust.Soc.Am. **99**, 3334 (1996).

[28] R.A.Guyer, K.R.McCall, G.N.Boitnott, "Hysteresis, discrete memory and nonlinear elastic wave propagation in rock", Phys.Rev.Lett. **74**, 3491-3494 (1995).

[29] J.A.TenCate, T.J.Shankland, Geophys.Res.Lett. **23**, 3019-3022 (1996).

[30] J.A.TenCate, E.Smith, R.A.Guyer, Phys.Rev.Lett. **85**, 1020-1024 (2000).

[31] K.R.McCall, R.A.Guyer, Nonlinear Processes in Geophysics **3**, 89-101 (1996).

[32] K.Van Den Abeele, P.A.Johnson, R.A.Guyer, K.R.McCall, J.Acoust.Soc.Am. **101**, 1885-1898 (1997).

[33] F. Cleri, Comput. Mat. Science, in press.

[34] F.Cleri, S.Yip, D.Wolf, S.R.Phillpot, Phys.Rev.Lett. **79**, 1309-1312 (1999).

[35] M. Scalerandi, E. Ruffino, P.P.Delsanto, P.A.Johnson, K. Van Den Abeele, in "Review of Progress in Quantitative Non Destructive Evaluation", vol. **19**B, ed. by D.O.Thompson and D.E.Chimenti, (Melville, AIP Conference Proceedings, 2000), 1393-99.

[36] E.Ruffino, M.Scalerandi, Il Nuovo Cimento B **115**, 645-652 (2000).

[37] R.A.Guyer, K.R.McCall, G.N.Boitnott, L.B.Hilbert, T.J.Plona, J.of Geoph.Res. **102**, 5281 (1997).

[38] D.E.Smith. J.A.TenCate, Geoph.Res.Lett. **27**, 1985 (2000).

[39] K.Van Den Abeele, P.A.Johnson, A.Sutin, Research in Nondestructive Evaluation **12**, 17-30 (2000).

[40] P.P.Delsanto, V.Agostini, M.Scalerandi, P.A.Johnson, *Phenomenology and modeling of damaged mesoscopic materials*, to appear in the Proccedings of EuroMech Conference (Prague, september 2000).